Geophysical Journal International

Geophys. J. Int. (2024) **238,** 346–363
Advance Access publication 2024 May 8
GJI Seismology

https://doi.org/10.1093/gji/ggae164

The expression of mantle seismic anisotropy in the global seismic wavefield

Jonathan Wolf[1], Maureen D. Long,[1] Daniel A. Frost[2] and Tarje Nissen-Meyer[3]

[1]*Department of Earth and Planetary Sciences, Yale University, New Haven, CT* 06511, *USA. E-mail: jonathan.wolf@yale.edu*
[2]*School of the Earth, Ocean and Environment, University of South Carolina, Columbia, SC* 29208, *USA*
[3]*Department of Earth Sciences, University of Oxford, Oxford OX*1 3*AN, UK*

Accepted 2024 May 7. Received 2024 February 3; in original form 2023 May 18

SUMMARY

The dependence of seismic wave speeds on propagation or polarization direction, called seismic anisotropy, is a relatively direct indicator of mantle deformation and flow. Mantle seismic anisotropy is often inferred from measurements of shear-wave splitting. A number of standard techniques to measure shear-wave splitting have been applied globally; for example, ∗KS splitting is often used to measure upper mantle anisotropy. In order to obtain robust constraints on anisotropic geometry, it is necessary to sample seismic anisotropy from different directions, ideally using different seismic phases with different incidence angles. However, many standard analysis techniques can only be applied for certain epicentral distances and source–receiver geometries. To search for new ways to detect mantle anisotropy, instead of focusing on the sensitivity of individual phases, we investigate the wavefield as a whole: we apply a 'wavefield differencing' approach to (systematically) understand what parts of the seismic wavefield are most affected by splitting due to seismic anisotropy in the mantle. We analyze differences between synthetic global wavefields calculated for isotropic and anisotropic input models, incorporating seismic anisotropy at different depths. Our results confirm that the seismic phases that are commonly used in splitting techniques are indeed strongly influenced by mantle anisotropy. However, we also identify less commonly used phases whose waveforms reflect the effects of anisotropy. For example, PS is strongly affected by splitting due to seismic anisotropy in the upper mantle. We show that PS can be used to fill in gaps in global coverage in shear-wave splitting data sets (for example, beneath ocean basins). We find that PcS is also a promising phase, and present a proof-of-concept example of PcS splitting analysis across the contiguous United States using an array processing approach. Because PcS is recorded at much shorter distances than ∗KS phases, PcS splitting can therefore fill in gaps in backazimuthal coverage. Our wavefield differencing results further hint at additional potential novel methods to detect and characterize splitting due to mantle seismic anisotropy.

Key words: Numerical modelling; Planetary interiors; Computational seismology; Seismic anisotropy; Wave propagation.

1 INTRODUCTION

Mantle deformation induced by convective mantle flow manifests itself in seismic anisotropy (e.g. Long & Becker 2010). Seismic anisotropy denotes the dependence of seismic wave speeds on the propagation or polarization direction of the wave. It has been demonstrated that seismic anisotropy is particularly strong in the boundary layers of mantle convection, while it is almost absent in the bulk of the lower mantle (e.g. Meade *et al.* 1995; Niu & Perez 2004; French & Romanowicz 2014). In particular, seismic anisotropy has been detected in the upper mantle (e.g. Silver 1996; Savage 1999; Becker & Lebedev 2021), the mantle transition zone (e.g. Yuan & Beghein 2014; Chang & Ferreira 2019), the uppermost lower mantle (e.g. Foley & Long 2011; Lynner & Long 2015; Mohiuddin *et al.* 2015; Chang & Ferreira 2019), and the lowermost mantle (e.g. Wookey *et al.* 2005; Nowacki *et al.* 2010; Creasy *et al.* 2017; Wolf *et al.* 2023c); summarized by Wolf *et al.* (2024a). In general, the deeper seismic anisotropy is located in the mantle, the more difficult it is to resolve it with body wave approaches (Wolf *et al.* 2022b). Despite these challenges, however, a thorough picture of mantle anisotropy across all depths would be helpful to understand global patterns of mantle deformation and flow (e.g. Becker & Lebedev 2021).

Seismic anisotropy manifests itself in the seismic wavefield in a number of ways, and there are several analytical techniques used

to detect and characterize it. Anisotropy in Earth's crust and upper mantle can be measured using receiver function analysis (e.g. Levin & Park 1997; Schulte-Pelkum *et al.* 2005; Nikulin *et al.* 2009; Haws *et al.* 2023) or surface wave tomography (e.g. Panning & Nolet 2008; Ferreira *et al.* 2010; Zhu *et al.* 2020). Waveform inversion techniques have also been developed to characterize radial anisotropy in the mantle (e.g. Kawai & Geller 2010; Suzuki *et al.* 2021). Probably the most commonly used method to study seismic anisotropy in Earth's mantle, and the one we focus on in this paper, invokes measurements of so-called shear-wave splitting (e.g. Long & Silver 2009). The distribution of shear wave energy away from its initial polarization direction, splitting the wave into two quasi-shear waves, is indicative of seismic anisotropy (e.g. Silver & Chan 1991).

Depending on which portion of the mantle is being studied, different shear phases (or combinations of phases) are typically used. Fig. 1(a) summarizes most commonly used seismic phases for the analysis of mantle anisotropy using shear-wave splitting. To analyze seismic anisotropy in the upper mantle directly beneath the receiver, the most commonly used phase is SKS, sometimes supplemented with SKKS and PKS (e.g. Silver & Chan 1991; Chevrot 2000; Liu *et al.* 2014; Walpole *et al.* 2014; Graw & Hansen 2017; Lopes *et al.* 2020). For such an analysis of upper mantle anisotropy, it is often assumed that the influence of lowermost mantle anisotropy is negligible. An alternative and commonly applied approach to studying upper mantle anisotropy is to infer source-side anisotropy from splitting of teleseismic *S* waves using explicit receiver-side anisotropy corrections (e.g. Russo & Silver 1994; Lynner & Long 2013; Walpole *et al.* 2017; Eakin *et al.* 2018). Source-side direct *S* splitting can also be used to study transition zone and uppermost lower mantle anisotropy in places where deep earthquakes occur (e.g. Foley & Long 2011; Mohiuddin *et al.* 2015). These observational strategies are well-established and have been used to map upper mantle anisotropy across much of Earth's landmasses. Beneath the oceans, however, shear-wave splitting constraints on upper mantle anisotropy are sparse (e.g. IRIS DMC 2012), due to the paucity of seismic receivers.

Lowermost mantle anisotropy is generally more challenging to measure than seismic anisotropy in the upper mantle. A major reason for this is that all seismic waves that may sample seismic anisotropy in the lowermost mantle also travel through the upper mantle, potentially accumulating an upper mantle splitting signal before they reach the station (Fig. 1a). Different measurement strategies have been developed to distinguish between an upper and lowermost mantle contribution. Such techniques include the analysis of differential S-ScS splitting (e.g. Wookey *et al.* 2005; Nowacki *et al.* 2010; Creasy *et al.* 2017; Wolf *et al.* 2019), and differential splitting of SKS and SKKS (e.g. Niu & Perez 2004; Deng *et al.* 2017; Grund & Ritter 2018; Reiss *et al.* 2019; Tesoniero *et al.* 2020; Asplet *et al.* 2020). An alternative technique makes use of the long ray path of S_{diff} through the lowermost mantle, inferring deep mantle anisotropy by measuring splitting of S_{diff} (e.g. Vinnik *et al.* 1989, 1995; Cottaar & Romanowicz 2013; Wolf & Long 2023b; Wolf *et al.* 2023b, 2024b), typically comparing with SKS splitting to account for any upper mantle contributions.

The sensitivity of seismic body wave phases to mantle seismic anisotropy is often investigated on a phase-by-phase basis, sometimes by applying splitting techniques to synthetic seismograms that were calculated for known Earth input models (e.g. Nowacki & Wookey 2016; Wolf *et al.* 2022b). Other times, the sensitivity of individual seismic phases in an anisotropic Earth is investigated by calculating sensitivity kernels (e.g. Favier *et al.* 2004; Sieminski *et al.* 2007, 2008). While such approaches are very helpful for a detailed understanding of how and where individual phases are affected by seismic anisotropy, they only focus on a fraction of the seismic wavefield. In this study, we aim for a systematic search of the seismic wavefield in order to uncover novel splitting strategies. We implement a wavefield differencing approach that allows us to systematically analyze the effects of anisotropy on the entire seismic wavefield, and to investigate which phases are most sensitive to anisotropy in which portions of the mantle.

While commonly used shear-wave splitting strategies using phases such as SKS, SKKS and ScS continue to yield valuable information on anisotropy at various depths in the mantle, they all have limitations, including those imposed by the distribution of seismic stations and earthquakes at the relevant distance ranges. Expanding the repertoire of seismic body wave phases that can be used for shear-wave splitting analysis is desirable, as this would allow for splitting data sets with better spatial and azimuthal coverage. In service of this goal, in this study we carry out a systematic investigation of how seismic anisotropy located at different depths in the Earth's mantle expresses itself in the global seismic wavefield. We analyze a large number of body wave phases (Fig. 1), many of which are not routinely used for shear-wave splitting measurements. Our results point towards potential new (or rarely used) techniques to map upper mantle anisotropy using shear-wave splitting, including those that rely on PS and PcS phases. We provide proof-of-concept examples of these strategies applied to real data and discuss how they might improve our ability to image anisotropy, deformation, and flow in the Earth's mantle.

2 WAVEFIELD DIFFERENCING: METHODS AND APPROACH

2.1 Global wavefield simulations

We conduct global wavefield simulations using AxiSEM3D (Leng *et al.* 2016, 2019), which is capable of handling any 3-D input model and arbitrary seismic anisotropy (Tesoniero *et al.* 2020). In this work, we focus on axisymmetric simulations, for which AxiSEM3D is as efficient as its older relative AxiSEM (Nissen-Meyer *et al.* 2014). We compute global wave propagation simulations down to ∼5 s period using AxiSEM3D, following the methodology applied in previous work (e.g. Wolf *et al.* 2022a). We always use a smoothed version of isotropic PREM (Dziewonski & Anderson 1981, see below) as our background model and always consider (PREM-) attenuation as well as Earth's ellipticity. We intentionally keep our input models simple to generally assess where in the seismic wavefield seismic anisotropy manifests itself. Effects of laterally changing seismic anisotropy and 3-D input models have been addressed in previous work (e.g. Wolf *et al.* 2022a, b).

The typical source–receiver configuration for our simulations is shown in Fig. 2(a). We place our 100 m deep seismic source at the North Pole, simulating either a normal or strike-slip fault earthquake (Fig. 2a). The very shallow focal depth helps to avoid surface reflections (depth phases) in our seismograms. We select two different focal mechanisms (Fig. 2a); their details are only important inasmuch as they influence the initial polarization of the seismic wave. The stations are spaced on a regular 2-degree latitude–longitude grid, leading to a closer station spacing at the poles than at the equator (Fig. 2a). This configuration ensures that stations are regularly spaced along the azimuthal direction.

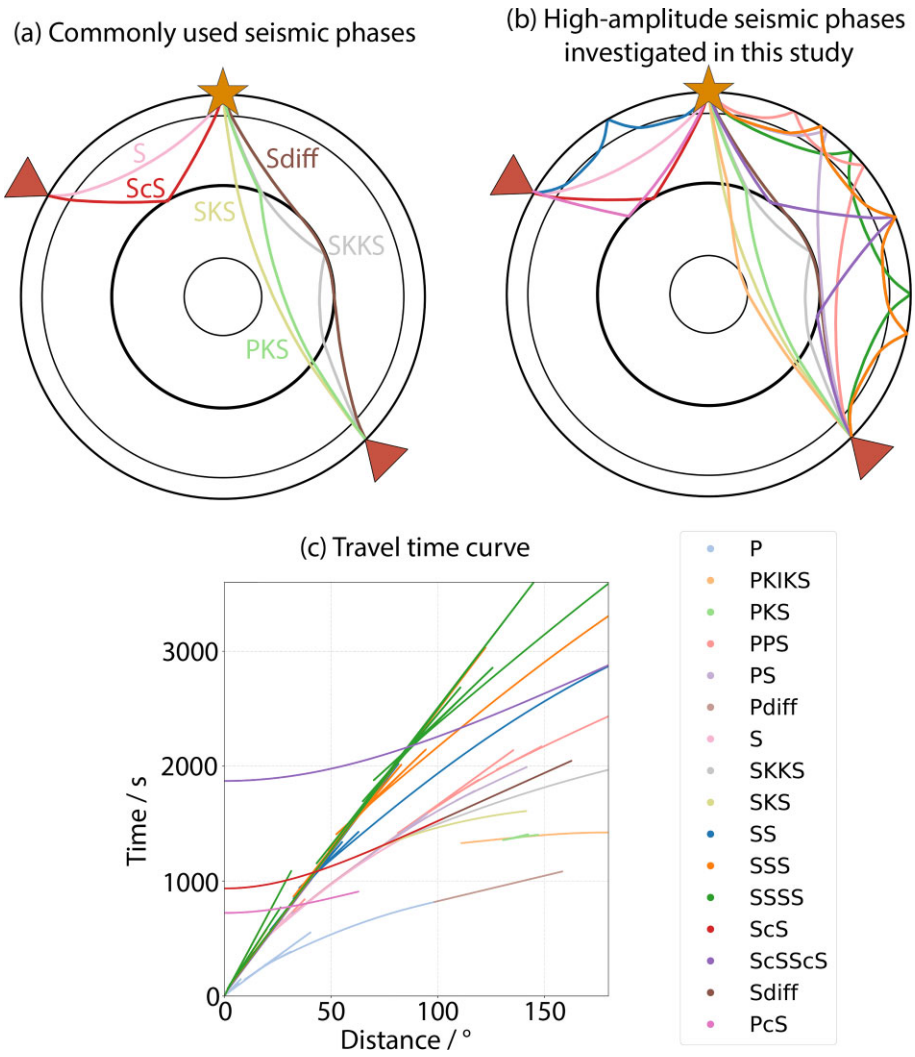

Figure 1. Seismic phases used and this study and their traveltimes. (a) Ray path sketch for seismic phases commonly used to infer upper (SKS, SKKS and PKS) and lowermost (SKS, SKKS, *S*, ScS and S_{diff}) mantle anisotropy. (b) Seismic phases that usually have high amplitudes in seismograms investigated in this study. See legend for color key. (c) Traveltime curve for all seismic phases presented in panel (b), using the same colors. The traveltime curve was calculated for a 100 m deep event, as used in the global wavefield simulations.

We implement seismic anisotropy in our models by replacing the smoothed PREM velocity input model by seismic anisotropy described by a horizontally transversely isotropic (HTI) elastic tensor created using MSAT (Walker & Wookey 2012). We consider five different models, each with anisotropy in a different depth range. The depth ranges of anisotropy that we investigate are 24–220 km (layer 1), 220–400 km (layer 2), 400–670 km (layer 3), 670–800 km (layer 4) and 2641–2891 km (layer 5), as shown in Fig. 2(b). We ensure that the isotropic average of the anisotropy used in each of these layers agrees with our smoothed isotropic PREM model, for which velocities are constant within each layer. The anisotropic strength within our lowermost mantle layer (layer 5) is 2.75 per cent; we adjust the anisotropic strength in each of the other layers such that we would obtain the same splitting delay time (∼1 s) for each of them for a vertically incident wave. We implement two different elastic tensor arrangements (Figs 2c and d), representing crystallographic preferred orientation of olivine: in one, the direction from which the elastic tensor is sampled changes with azimuth (arrangement 1; Fig. 2c), while in the other it is always the same (arrangement 2; Fig. 2d). We implement these two different elastic tensor arrangements to ensure that our results are not strongly affected by the specific direction that the seismic anisotropy is sampled from. Whenever we use the seismograms to calculate *absAD* and *relAD* (see below), we cannot output seismograms for all stations from our source-station setup (Fig. 2a) at an appropriate sampling period (1 s) due to storage limitations. Instead, we output seismograms every 15° azimuth and every 2° distance.

2.2 Data processing

In order to understand how seismic anisotropy expresses itself, we compare the seismic wavefield computed for our isotropic input model with the wavefields from each of our anisotropic simulations. Specifically, we compute the displacement U_i or **U**, the gradient of displacement D_{ij} or **D**, the curl of displacement R_i or **R**, stress S_{ij} or **S**, and strain E_{ij} or **E**, where i,j = 1,2,3 correspond to the radial (1), transverse (2) and vertical (3) direction. The difference between the isotropic and the anisotropic simulations will be indicated with a δ-sign in the following, for example $\delta U_1 = U_{1,\,iso} - U_{1,\,ani}$. From this differential wavefield, we infer how much different seismic phases are influenced by mantle anisotropy. We can express this either in

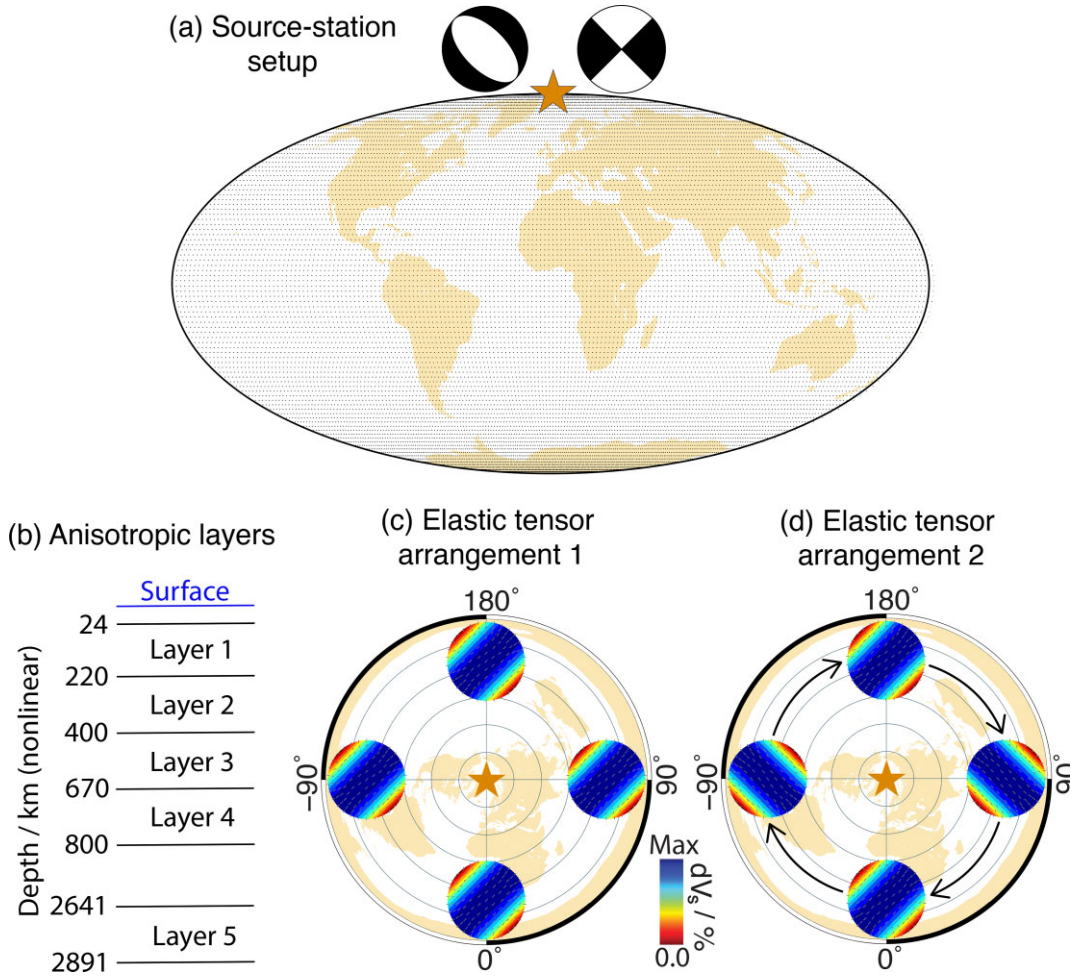

Figure 2. Setup for global wavefield simulations. (a) Source (yellow star) – station (black dots on map) configuration. Events either have a normal (left) or a strike-slip (right) geometry (top). (b) Depths at which we incorporate seismic anisotropy into our AxiSEM3D input models. Layer 1: Upper mantle; layer 2: lower upper mantle; layer 3: transition zone; layer 4: upper lower mantle; layer 5: lowermost mantle. (c) Elastic tensor arrangement 1. The source is represented as a yellow star on the map, which uses a north pole centered projection, and the horizontally transversely isotropic elastic tensors are shown as stereoplots. For elastic tensor arrangement 1, the direction from which the elastic tensor is sampled changes as a function of azimuth. (d) Elastic tensor arrangement 2, presented using the same plotting conventions as in panel (c). For elastic tensor arrangement 2, the direction from which the elastic tensor is sampled is the same for every azimuth.

terms of a scalar quantity that explicitly considers the amplitude of the incoming wave, or as a scalar quantity that is normalized to the amplitude. To do this, we derive the phase-specific absolute and relative normalized integrated apparent difference (*absAD* and *relAD*) from the delta field. For U_1 and the SS seismic phase *absAD* can be expressed as:

$$absAD_{U_1,SS} = \sum_{a=0^\circ}^{180^\circ} \sum_{d=d1>20^\circ}^{d2\leq 180^\circ} \sum_{t=tSS}^{tSS+20} |\delta(U_1^{a,d,t})|/(d2-d1)\,, \qquad (1)$$

where a denotes the azimuth index, $d1$ is the shortest distance at which the phase arrives (but always $>20^\circ$), $d2$ is the largest distance at which the phase arrives (but always $\leq 180^\circ$), d is the distance index, *tSS* is the phase arrival time for the SS phase, and t the time index. Therefore, *absAD* quantifies how much a particular phase is influenced by mantle anisotropy by analyzing the 20 s after the phase onset, integrating over distance and azimuth and normalizing the value by the distance range over which the phase occurs. We find a time interval length of 20 s especially useful for the more attenuated phases with a relatively long dominant period. Similarly, it can be calculated how much a particular phase is affected by mantle anisotropy relative to its isotropic amplitude. This quantity is

$$relAD_{U_1,SS} = \sum_{a=0^\circ}^{180^\circ} \sum_{d=d1>20^\circ}^{d2\leq 180^\circ} \left(\max\left(\left|U_{iso}^{d,t=1,2,\ldots,20}\right|\right)\right)^{-1} \sum_{t=tSS}^{tSS+20} |\delta(U_1^{d,t})|/(d2-d1)\,, \qquad (2)$$

where U_{iso} denotes the displacement amplitude in the isotropic seismogram. *absAD* and *relAD* will also be calculated for D_{ij}, R_i, S_{ij} and E_{ij} in addition to displacement U_{ij}.

For the interpretation of *absAD* and *relAD*, it is important to note that we do not explicitly consider phase interference in the calculations, but simply use the 20 s after the phase arrivals whether or not another seismic phase arrives in this time window. Moreover, the contribution to *absAD* is stronger at shorter distances as $|\delta U_i|$ will be larger due to geometric spreading. This is not the case for *relAD*. Therefore, phases for which *absAD* is large likely have large amplitudes for at least a certain distance range and are, at the same time, sensitive to seismic anisotropy. Phases for which *relAD* is large

do not necessarily have high amplitudes but are strongly indicative of seismic anisotropy.

3 WAVEFIELD DIFFERENCING RESULTS

3.1 Exploring the full seismic wavefield

To visualize the difference in seismic wave propagation between isotropic and anisotropic simulations, we create movies showing its time evolution. Example snapshots from such movies are shown in Fig. 3 for seismic anisotropy in the upper mantle (upper panel) and the lowermost mantle (lower panel). We also provide Movies S1–S5 that show the time evolution of the differential wavefield for elastic tensor arrangement 1 and seismic anisotropy at different depths (layers 1–5). The overall wavefield difference is substantially more affected by upper mantle anisotropy due to its influence on surface waves. The influence of surface waves becomes less the deeper in the mantle the seismic anisotropy is placed. In the difference snapshots for lowermost mantle anisotropy, different body wave phases that are often used to characterize it can be very well distinguished (e.g. SKS, SKKS, ScS and S_{diff}). The patterns that are apparent for upper and lowermost mantle anisotropy on a wave front along a particular distance away from the source are a combination of the initial source polarization and the sampling of the elastic tensor from an azimuth-dependent direction (arrangement 1).

While these wavefield difference movies are informative, they mainly visually emphasize the phase arrivals that are most affected by mantle seismic anisotropy at each point in time. To also focus on less affected phases, we investigate the differential wavefield at a particular azimuth, plotted on top of a traveltime curve (Fig. 4 for upper mantle and transition zone; Fig. 5 for the lower mantle). Fig. 4 demonstrates that, as expected, the deeper the anisotropy is placed in the upper mantle, transition zone, or uppermost lower mantle (layers 1–4), the weaker its influence on near surface reverberations and on surface waves. Phases that are strongly influenced by seismic anisotropy in layers 1–4 include, for example, SS, SSS and SSSS; in fact, these phases are affected so strongly that the difference plots show their minor arc siblings as features with an opposite moveout (upper right-hand corner).

These results for layers 1–4 can be compared to those for layer 5 (lowermost mantle anisotropy; Fig. 5). The magnitude of the wavefield differences depends on azimuth, but the absolute sensitivity of each seismic phase to lowermost mantle anisotropy is the same for all azimuths. Seismic phases that are primarily influenced by lowermost mantle anisotropy include the phases commonly used to infer its presence (e.g. ScS, S_{diff}, SK(K)S), but also ScSScS and ScSScSScS. Moreover, at certain distances (P)PS seems to be influenced by lowermost mantle anisotropy, likely because it is sampling the lowermost mantle at these distances and merging with (P)PScS (analogous to S/ScS at ∼90–100°). The details of the differential wavefield (unsurprisingly) depend on the focal mechanism and the elastic tensor arrangement (Figs S1–S4). The overall patterns, however, are the same for all of these scenarios.

3.2 Influence of seismic anisotropy on individual seismic phases

Next, we calculate *absAD* (Fig. 1) for various seismic phases, which shows us how strongly absolute phase amplitudes are affected by mantle anisotropy. These results are shown for δU_i in Fig. 6 and for D_{ij}, R_i, S_{ij} and E_{ij} in Figs S5–S12. As expected from the patterns in Figs 4 and 5, similar phases are affected by seismic anisotropy in layers 1–4, whereas the phases mainly influenced by lowermost mantle anisotropy (layer 5) are different. It is unsurprising that *S*, SS, SSS and SSSS are strongly affected by upper mantle anisotropy since they travel through the upper mantle two or more times. We find that the transverse components (U_2) of SK(K)S phases are particularly affected by mantle anisotropy. This is expected since SK(K)S would be SV-polarized in an isotropic Earth due to the P-SV conversion at the CMB. Indeed, this insight underpins the popularity of SK(K)S splitting as a tool for measuring anisotropy. The fact that PKIKS and PKS seem largely unaffected by mantle anisotropy in this view has to do with the strike-slip focal mechanism used for the simulation (compare to Fig. S6); this is therefore a function of the radiation pattern, rather than an actual lack of sensitivity to anisotropy.

Our calculation of *absAD* for different phases can shed light on whether there are body wave phases that are strongly affected by mantle anisotropy that are not typically used in splitting studies. Such phases, which are strongly affected by seismic anisotropy in layers 1–4 in all simulations (Figs 6a–d and Figs S5–S12) include PS and PPS. This is especially noteworthy because their polarization is determined by the *P*-SV conversion through of the surface underside reflection, which makes them much easier to analyze than, for example, SS. We also find that PcS is strongly influenced by upper mantle anisotropy in our simulations. This is partially due to the interference with *S* at some of the distance range, but in general, PcS splitting is analogous to ∗KS splitting, although PcS usually has smaller amplitudes (e.g. Liu & Grand 2018). For the lowermost mantle case, we find that anisotropy mostly affects SKS, SKKS and ScS phases (Fig. 6e) and no unusual phases that are strongly affected by deep mantle anisotropy, but rarely used to infer its presence, are immediately apparent.

So far, we have analyzed how much seismic phases are affected by mantle anisotropy in terms of absolute amplitude. Results for relative amplitude or *relAD* are shown in Fig. 7 for δU_i. Fig. 7 shows that for each layer, transverse components are particularly affected for phases that travel through the outer core and convert from *P* to SV at the CMB. This is logical because in the isotropic case transverse component energy is not present in the absence of phase interference. (Note that to avoid dividing by zero, we add a water level divisor to our calculations). Seismic anisotropy in layers 1–4 tends to affect S, SS, SSS and SSSS increasingly strongly, since the higher multiples sample seismic anisotropy more often. For the lowermost mantle, prominent signals for PKS and ScSScS are visible for *relAD* which were less apparent for *absAD* in Fig. 5(e).

Interestingly, the influence of seismic anisotropy in layers 2–4 on each individual seismic phase is similar (Figs 6 and 7). One reason for this is that for these three layers the influence of the anisotropy on surface waves and near surface reverberations is substantially lower than for layer 1. At the same time, layers 2–4 are sampled from a similar incidence angle for most phases, while the angle at which layer 5 is sampled can be very different. By construction, the strength of anisotropy sampled by a vertically incident seismic wave is the same in each layer (Section 2.1), and many phases sample layers 2–4 close to vertical for most distances. Therefore, the anisotropic signature of splitting due to anisotropy in each of those three layers that is visible in individual phases is comparable.

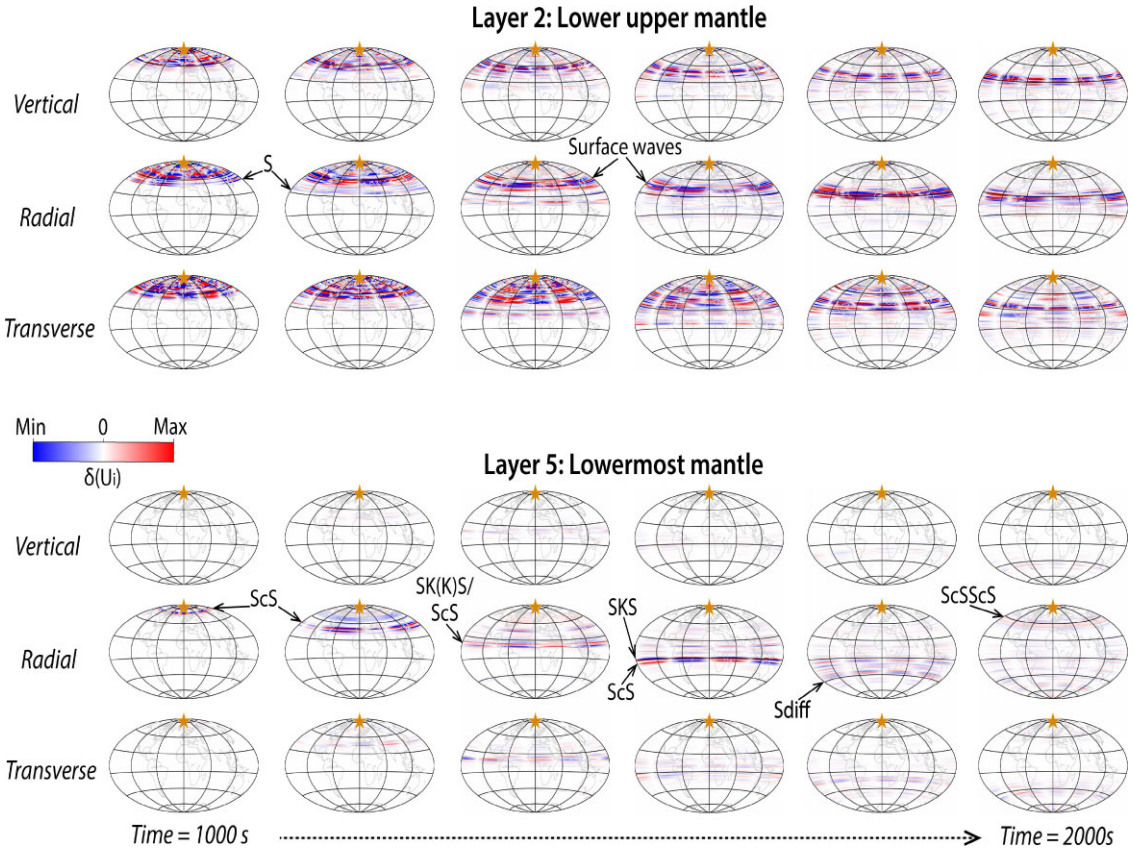

Figure 3. Time snapshots of the differential displacement wavefield (see color bar) for vertical, radial and transverse components from 1000 s (left) to 2000 s (right) after event origin time, for elastic tensor arrangement 1. The top panel shows δU_i for seismic anisotropy in the lower upper mantle and the bottom panel for the lowermost mantle. Different seismic phases are marked on the snapshots.

4 DISTINGUISHING ANISOTROPY AND HETEROGENEITY AND THE IMPORTANCE OF SHEAR-WAVE SPLITTING

The results shown in Figs 3–7 demonstrate that anisotropy has a significant effect on the global seismic wavefield. However, it also well known that isotropic widespread heterogeneity significantly affects the seismic wavefield. A key question, therefore, is how to distinguish the effects of anisotropy and heterogeneity. Here, we use a set of simulations that incorporate isotropic heterogeneity (as expressed in a global mantle tomography model) to illustrate the well-established principle that measurements of shear wave splitting can be used as a clear indicator of seismic anisotropy.

We first review the well-established theoretical basis for shear wave splitting observations (Vinnik *et al.* 1989a; Silver & Chan 1991). For simplicity, we assume an SV-polarized wave before it samples seismic anisotropy, such as any shear wave which has undergone a P-to-SV conversion (e.g. SKS). We can describe this wave as a harmonic wave with the angular frequency ω. Assuming that $\omega t << 1$ (with t being time), the radial component $R(t)$ can be expressed as

$$R(t) \simeq \cos \omega t \tag{3}$$

(Vinnik *et al.* 1989a; Silver & Chan 1991). After traveling through the anisotropic material, the transverse component $T(t)$ will have the shape of the radial component time derivative $R'(t)$

$$T(t) \simeq -0.5\omega\delta t \sin 2(\alpha - \phi) \sin \omega t = 0.5\omega\delta t \sin 2(\alpha - \phi) R'(t) , \tag{4}$$

where δt is the time lag between the split waves, ϕ is the fast polarization direction (measured clockwise from the north direction) and α is the backazimuth (which is the same as the initial polarization) for core-refracted phases such as SKS.

A quantity that is also useful to introduce is the splitting intensity (Chevrot 2000), *SI*, defined as

$$SI = -2\frac{T(t)R'(t)}{|R'(t)|^2} \approx \delta t \sin(2(\alpha - \phi)) . \tag{5}$$

The splitting intensity is high if two conditions are met: First, the transverse component has a significant amplitude and, second, the radial time derivative has the shape of the transverse component. Eq. (4) illustrates that both is true in case of shear-wave splitting due to seismic anisotropy.

We carry out a set of simulations that illustrates why shear-wave splitting is such a powerful tool for distinguishing the effects of seismic anisotropy and 3-D heterogeneity. We perform three types of simulations using the setup shown in Fig. 8(a) with a 600 km deep source and otherwise the same parameters as described in Section 2.1. First, we calculate seismic wave propagation using isotropic PREM as background model. Secondly, we also implement seismic anisotropy in layer 2 (Fig. 2b); and, third, we replace

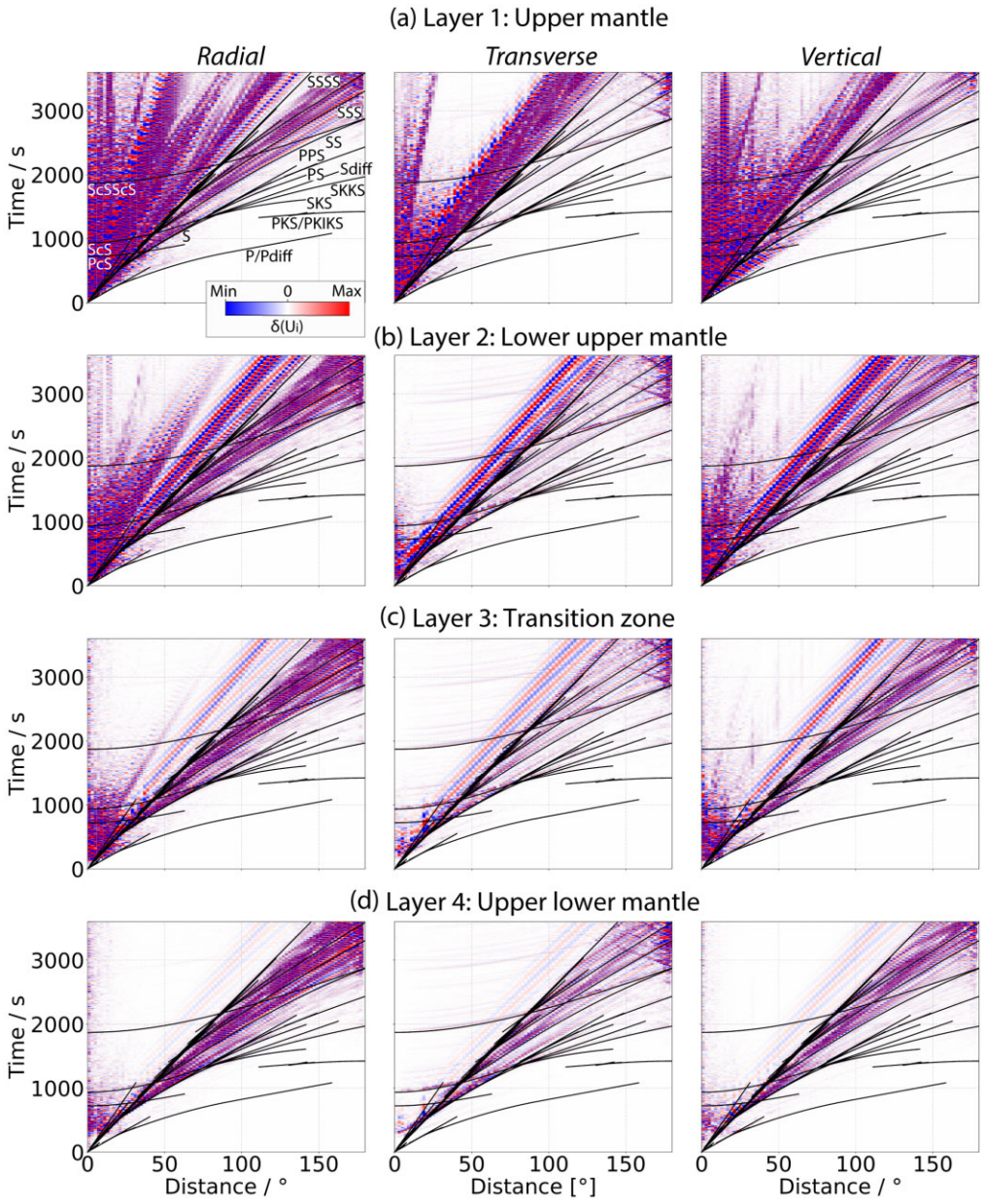

Figure 4. Differential displacement wavefield (color bar) as a function of distance for an azimuth of 0°, calculated using a strike-slip source and elastic tensor arrangement 1 (Fig. 2c). (a) The differential wavefield for seismic anisotropy in layer 1 (upper mantle) is plotted underneath the traveltime curve shown in Fig. 1(c) with the phase traveltimes shown as black lines. The wavefield difference is presented for radial (left), transverse (middle) and vertical (right) components. (b) Same as panel (a) for seismic anisotropy in layer 2 (lower upper mantle). (c) Same as panel (a) for seismic anisotropy in layer 3 (transition zone). (d) Same as panel (a) for seismic anisotropy in layer 4 (upper lower mantle). White vertical stripes are due to the plotting convention are not to be interpreted.

the PREM mantle by the 3-D tomography model S40RTS without incorporating seismic anisotropy. The results of these simulations are shown in Fig. 8.

SKS waveforms (Fig. 8b) illustrate that while 3-D tomography shifts the SKS arrival time quite significantly, it does not lead to effects that mimic splitting: No significant transverse component energy is observed for either isotropic scenario, which is why splitting intensities are negligible. For seismic anisotropy in layer 2, however, the estimated splitting intensity is large (above 1). This is because the transverse component takes the shape of the radial component time derivative, causing an elliptical particle motion. The same is true for other ∗KS waves such as SKKS (Fig. 8c) and PKS (Fig. 8d). For seismic waves that are not SV polarized before sampling seismic anisotropy, the same argument can be made if the seismograms are simply rotated to the direction of initial polarization derived from the particle motion. This is shown for S (Fig. 8e) and SS (Fig. 8f) phases. For isotropic simulations, estimated splitting intensities are zero; in contrast, we observe splitting for the input model with seismic anisotropy.

These results show that, crucially, heterogeneity does not have the same effect as seismic anisotropy for different seismogram components and different seismic phases. Specifically, the waveform effects that seismic anisotropy has on different horizontal components make it distinguishable from isotropic effects through shear-wave

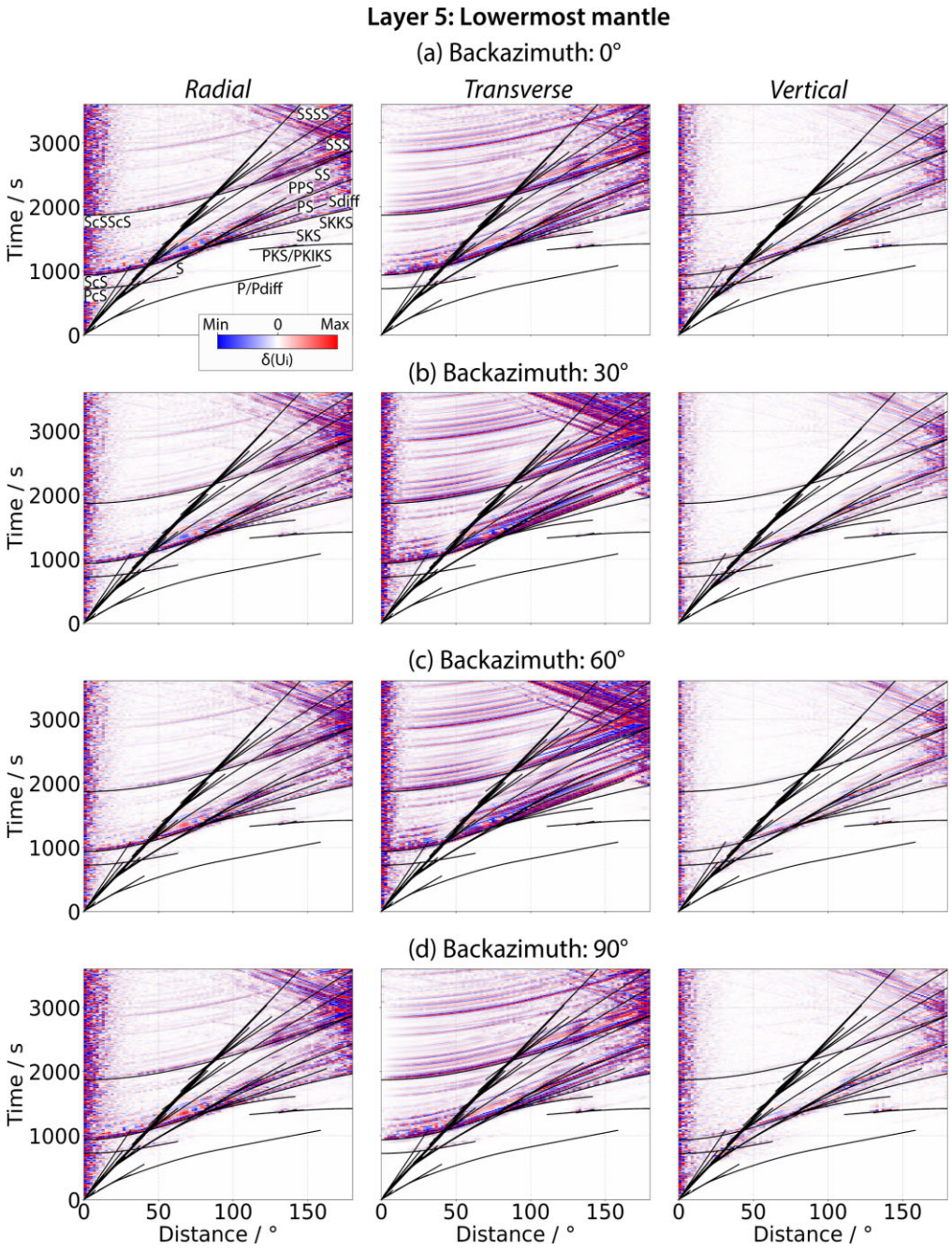

Figure 5. Differential displacement wavefield (color bar) as a function of distance for azimuths 0° (first row), 30° (second row), 60° (third row) and 90° (fourth row), calculated using a strike-slip source and elastic tensor arrangement 1 (Fig. 2c) for lowermost mantle anisotropy. Plotting conventions are as in Fig. 4.

splitting measurements. While time shifts caused by 3-D heterogeneity affect the overall seismic wavefield, these effects can be reliably distinguished from the effects of seismic anisotropy, as shown in Fig. 8(a). Our simulations therefore illustrate the well-established principle of shear-wave splitting can reliably distinguish between anisotropic effects and isotropic heterogeneity (e.g. Vinnik *et al.* 1989a; Silver & Chan 1991; Silver 1996; Romanowicz & Wenk 2017; Becker 2020).

We also calculate the differential displacement as in Figs 4 and 5 comparing simulations with isotropic PREM with a scenario in which the PREM-mantle is replaced by 3-D tomography (Fig. S13). This exercise is shown for completeness, although, strictly speaking, it is not directly comparable to our anisotropic simulations. The reason is that the main aspects that we consider when comparing displacements for two isotropic models (one of which includes realistic 3-D structure) are differential phase arrival times and waveforms distortions due to isotropic effects. Such effects were deliberately avoided in our anisotropic setup (for which the differential displacement is primarily influenced by the redistribution of energy for the horizontal components; Fig. 8). Thus, the differential displacement for the 3-D isotropic model (Fig. S13) is mostly influenced by two factors: the amplitude of the seismic wave (which also plays a role for the anisotropic simulations), and the path length travelled by the wave, which is approximately proportional to the traveltime (which, by construction, plays no role for the anisotropic simulations, except as it relates to the number of times

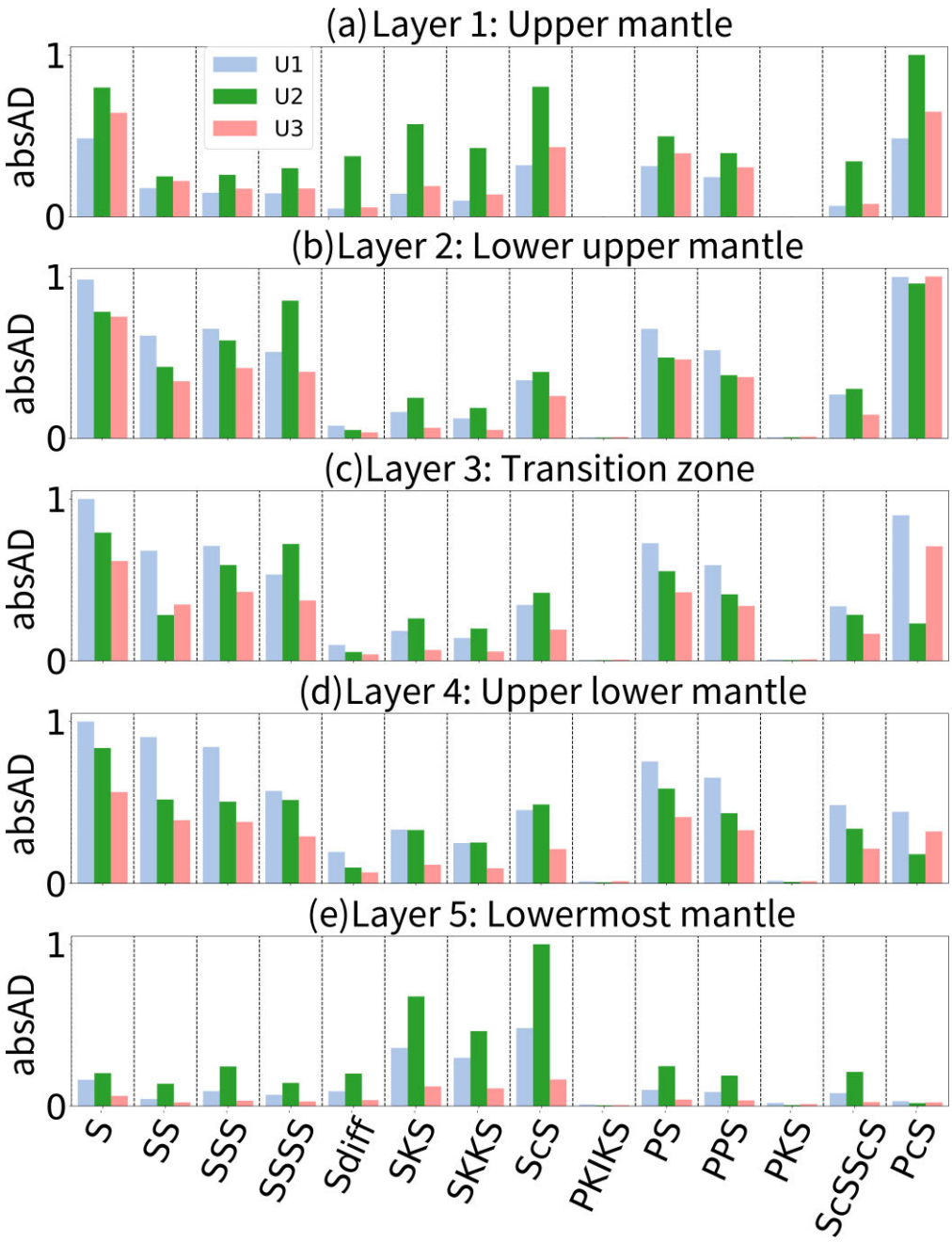

Figure 6. $absAD_{U_i}$ (see text) for radial (U_1, blue), transverse (U_2, green) and vertical (U_3, red) components for most seismic phases shown in Fig. 1(b). (a) $absAD_{U_i}$, normalized to the largest amplitude of either U_1, U_2 or U_3, for seismic anisotropy in layer 1 (upper mantle). b) Same as panel (a) for seismic anisotropy in layer 2 (lower upper mantle). (c) Same as panel (a) for seismic anisotropy in layer 3 (transition zone). (d) Same as panel (a) for seismic anisotropy in layer 4 (upper lower mantle). (e) Same as panel (a) for seismic anisotropy in layer 5 (lowermost mantle). For the calculation of $absAD_{U_i}$ and $relAD_{U_i}$ we sum over all calculated azimuths as laid out in eqs (1) and (2).

that an anisotropic layer is sampled). We account for the absolute amplitudes by calculating *relAD* for different seismic phases (Fig. S14). Unsurprisingly, the observed *relAD* values are much different than those for the anisotropic simulations (Fig. 7). While for the anisotropic simulations *relAD* is dominated by the redistribution of energy from one horizontal component to another, for the 3-D mantle model *relAD* values are much larger for radial and vertical components than for the transverse component. The reason for this is that *P* and SV waves are coupled while SH, which is recorded on the transverse component, travels independently (in isotropic media). Therefore, transverse waveforms are simpler for isotropic simulations and fewer differences are recorded. The results for the 3-D isotropic model comparison thus confirm the validity of our anisotropic wavefield differencing approach.

However, it is worth mentioning that there are known cases for which isotropic structure can mimic splitting, specifically for some reflected and diffracted seismic phases. The phases analyzed in Section 3.2 that are most affected by this complication are ScS (and its multiples) as well as S_{diff}. Detailed work on these phases has been conducted in past studies (Komatitsch *et al.* 2010;

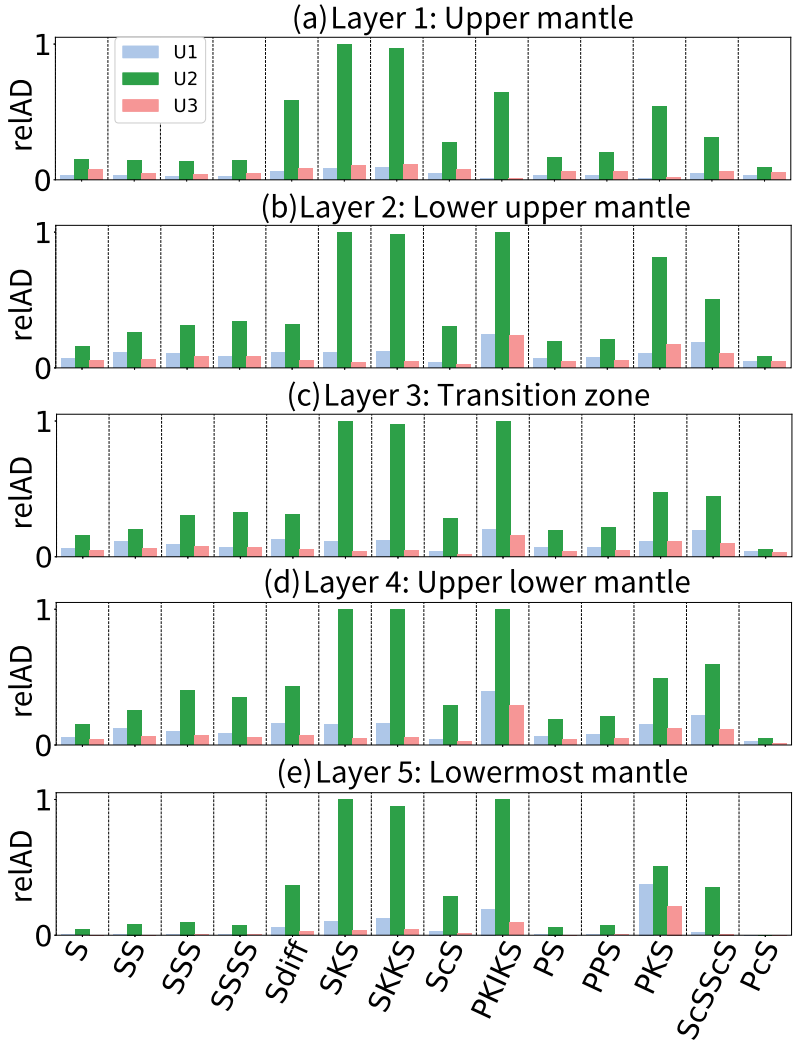

Figure 7. Same as Fig. 6 for $relAD_{U_i}$.

Borgeaud *et al.* 2016; Nowacki & Wookey 2016; Parisi *et al.* 2018; Wolf *et al.* 2023b; Wolf & Long 2024).

5 NOVEL SPLITTING STRATEGIES BASED ON WAVEFIELD DIFFERENCING RESULTS

5.1 Differential PS-SKS splitting: inferring upper mantle anisotropy close to the PS reflection point

We demonstrated in Section 3 that PS waves are strongly affected by seismic anisotropy in Earth's upper layers. For the purpose of splitting measurements, which are only sensitive to anisotropy structure along the path, PS is initially SV-polarized due to the P-to-S conversion upon reflection at the surface. It is worth pointing out that, because for the measurement of shear-wave splitting an S arrival at the receiver is needed, the order of *S* and *P* is generally not reversible (e.g. we could not measure SP splitting). On the S-leg of the ray path, PS samples seismic anisotropy in the upper mantle close to the reflection point as well as beneath the seismic receiver, and at distances between 90° and 115° any potential influence of lowermost mantle anisotropy can be avoided. Beneath the station, SKS samples seismic anisotropy in a very similar way as PS, such that differential PS-SKS splitting would point towards upper mantle anisotropy close to the PS reflection point at the surface (analogous to SKS-SKKS differential splitting for the lowermost mantle). Su & Park (1994) invoked this argument and measured seismic anisotropy in a location beneath the southwestern Pacific Ocean; however, this strategy has apparently not been used since. One possible reason for this is that there is no advantage to using the PS-SKS differential splitting technique when the alternative is to infer upper mantle anisotropy close to the potential reflection point by directly measuring SKS splitting at a seismic station located there. However, seismic stations are not regularly distributed across Earth's surface. Differential PS-SKS splitting is therefore potentially helpful to study anisotropy in regions that are sampled by PS bounce points but are not themselves well instrumented.

Here we present a proof-of concept example of PS-SKS splitting using real data. Before measuring PS and SKS splitting, we bandpass-filter our data, retaining periods between 6 and 25 s. To analyze seismic anisotropy, we use SplitRacer (Reiss & Rümpker 2017), a MATLAB-based graphical user interface. SplitRacer calculates the following shear-wave splitting parameters: the fast polarization (ϕ), the time delay time (δt) and the splitting intensity (SI; Chevrot 2000) of the split wave (Section 4). To measure the first

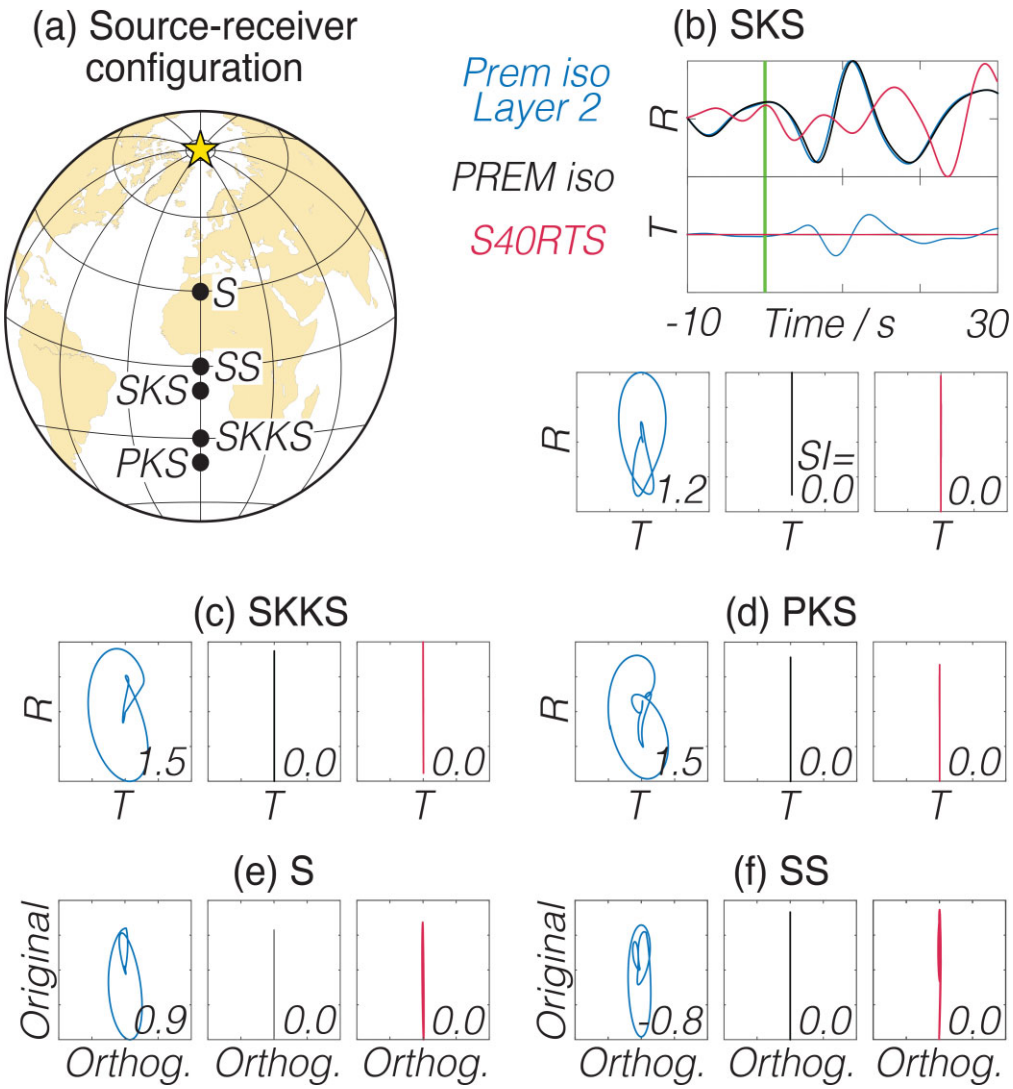

Figure 8. Representation of the differential effects that seismic anisotropy and 3-D velocity heterogeneity have on seismic waveforms. Results are from simulations that use (1) background model isotropic PREM (Dziewonski & Anderson 1981, black), (2) isotropic PREM and anisotropic layer 2 (blue) and (3) replacing the PREM-mantle by the tomography model S40RTS (Ritsema *et al.* 2011; red). (a) Source (yellow star) - receiver (black circles) configuration for phases S, SS, SKS, SKKS and PKS at randomly chosen distances at which they are recorded. (b) Top: SKS waveforms for all three types of simulations. Significant transverse component energy only arrives for the anisotropic simulations. 3-D heterogeneity shifts the arrival time compared to isotropic PREM. Bottom: Corresponding particle motions and *SI* values (bottom right in particle motion plots). *SI* values are 0 for isotropic simulations. (c) Particle motions and *SI* values for the SKKS phase. (d) Same as (c) for PKS. (e) Same as (c) for S. Note that particle motions are rotated in a coordinate system determined by the initial polarization of the wave. (f) Same as (e) for SS.

two quantities, SplitRacer uses the transverse energy minimization technique (Silver & Chan 1991) along with a corrected error formulation by Walsh *et al.* (2013). A strength of SplitRacer is that time windows are picked automatically, thereby ensuring that measurements are independent of a specific choice of time window.

We demonstrate a proof-of-concept example for PS-SKS splitting using station INK (Walpole *et al.* 2014) located in northeastern Canada, which exhibits null or nearly null SKS splitting over the entire backazimuthal range. Since INK is a null station (that is, a station that does not exhibit splitting due to upper mantle anisotropy beneath the receiver), any splitting contribution to PS waves must be caused by seismic anisotropy on the ray path far away from the station, most likely close to the PS reflection point at the surface. We analyze PS splitting parameters for events that occurred in the southeastern Pacific subduction zones between 10/1995 and 01/2023 at distances between 90° and 115°. Our results are shown in Fig. 9. We obtain ∼100 robust splitting intensity and two robust (ϕ, δt) measurements. We identify a strongly anisotropic region in the upper mantle to the north of Fiji, in which fast polarization directions are oriented approximately south–north (Fig. 9d). The PS waveforms and splitting diagnostic plots of the event (2009-01-19 03:35:18) are shown in Figs 9(a)–(c); this event was used to infer the (ϕ, δt) values for this strongly anisotropic region. Fig. 9(a) shows a clearly split PS phase, while the SKS phase for the same event is null. After correcting for the best-fitting PS splitting parameters (Fig. 9c), the corrected particle motion is linear (Fig. 9b), as expected in case of splitting due to seismic anisotropy.

Upper mantle anisotropy has been densely mapped beneath continents; however, for seismic anisotropy beneath ocean basins very little shear-wave splitting data are available (IRIS DMC 2012). To

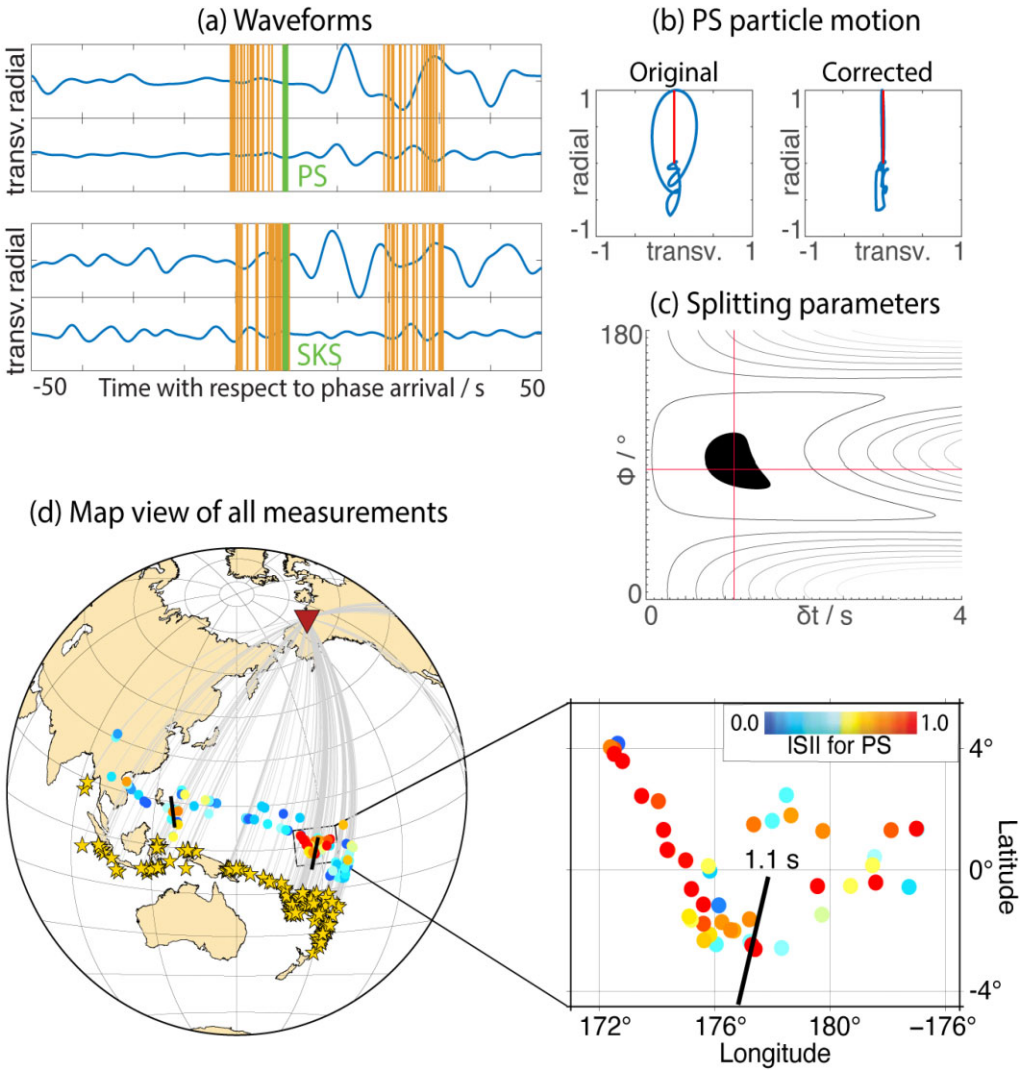

Figure 9. Differential PS-SKS splitting results for null station INK (Walpole *et al.* 2014). (a) PS (top) and SKS (bottom) radial and transverse component waveforms for an event that occurred on 01/19/2009. The PREM-predicted phase arrival time is shown with a green line and the start/end of the automatically selected measurement windows are shown with orange lines. SKS transverse energy is at the amplitude level of the noise; therefore, SKS splitting is null. (b) PS particle motions before (left) and after (right) correcting for the best fitting splitting parameters. (c) Best-fitting splitting parameters in the ϕ-δt plane. The 95 per cent confidence interval is shown in black, red crossing lines show the best fitting combination of (ϕ, δt). (d) Map view of the source (orange stars) – receiver (red triangle) configuration for the differential PS-SKS splitting analysis. Ray paths are shown as gray lines and colored circles indicate absolute PS splitting intensities (see legend). Black lines represent (ϕ, δt) splitting parameters. Bottom right: Zoom-in for the region of strong upper mantle anisotropy.

the extent that previous splitting measurements have been reported for the oceans, they were often made at ocean island stations (e.g. Fontaine *et al.* 2007), which themselves represent an anomalous tectonic setting, potentially influencing the upper mantle anisotropy beneath. Moreover, sometimes splitting measurements have been obtained through measurements of splitting from direct *S* waves (Mohiuddin *et al.* 2015; Eakin *et al.* 2018). Alternatively, some splitting measurements have been made using ocean bottom seismometers (e.g. Zietlow *et al.* 2014; Lynner 2021), which are expensive to install and typically yield relatively noisy data. We therefore recommend that the differential PS-SKS splitting technique be used systematically to map upper mantle anisotropy beneath oceans.

Building on this idea, we recently published an application of the differential PS-SKS splitting strategy suggested here to map seismic anisotropy beneath the Pacific Ocean basin (Wolf & Long 2023a), using a data set of ∼320 000 seismograms. This new work suggests that the PS-SKS differential splitting technique can also potentially be used for anisotropic tomography approaches (e.g. Mondal & Long 2020) to better resolve structure close to the PS bounce point.

5.2 PcS beam splitting: inferring upper mantle anisotropy near the receiver

Our results for *relAD* (Fig. 5) suggest that PcS is significantly affected by splitting due to mantle seismic anisotropy. However, due to its usually low amplitudes, PcS is not commonly used for the purpose of splitting measurements, with a few exceptions (e.g. Murdie & Russo 1999; He & Long 2011). Here, we apply a recently established beamforming technique to increase PcS signal-to-noise ratios and to measure splitting from the resulting beams.

To beamform PcS phase arrivals, we follow the methodology of Frost *et al.* (2024), using data from an event that occurred on 08/24/2011 in the Peru-Brazil border region (Fig. 10a). Wolf *et al.* (2023a) demonstrated that shear-wave splitting measurements from

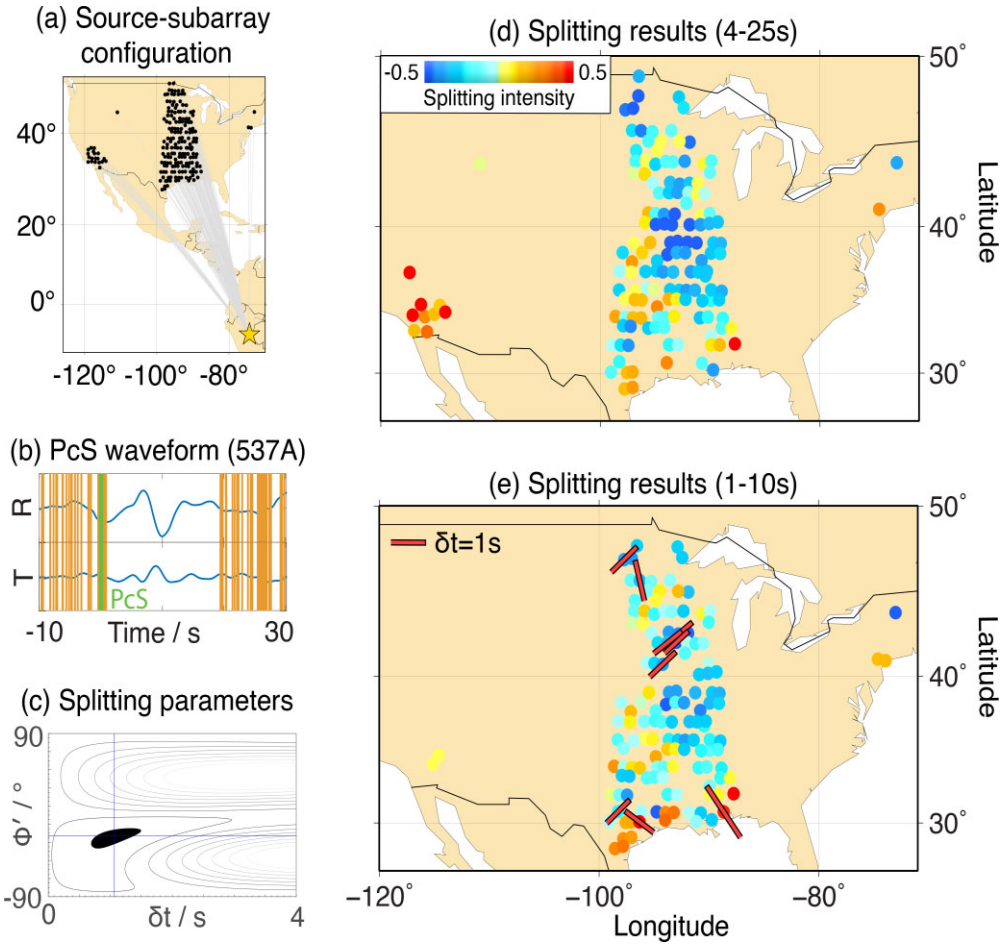

Figure 10. Summary of PcS beam splitting measurements. (a) The event used for the beamforming, which occurred on 08/24/2011, is represented as a yellow star (moment magnitude: 7.0; depth: 149 km). Subarray central stations across US are shown as black circles. (b) Radial (R) and transverse (T) component PcS beam waveforms for an example subarray with central station 537A. The PREM-predicted phase arrival time is shown by a green line and the start/end of the automatically selected measurement windows is presented by orange lines. (c) Best fitting splitting parameters (ϕ', δt) for the waveforms shown in panel (b). ϕ' denotes the fast polarization direction measured clockwise from the backazimuthal direction. The 95 per cent confidence interval is represented in black, with contour lines showing different transverse energy component levels. (d) Splitting measurements after applying a 4–25 s bandpass filter. Colors represent the splitting intensity (see legend), and are plotted a the central station location of each subarray. (e) Similar to panel (d) for a bandpass filter between 1 and 10 s. Nine well-constrained (ϕ, δt) measurements (red sticks) are obtained.

beamformed SK(K)S data reflect an average of the single-station splitting from the seismograms used for the beam. Therefore, PcS beam splitting is equivalent to a laterally averaged splitting contribution. Following Wolf *et al.* (2023a) and Frost *et al.* (2024), we construct subarrays of between 10 and 20 stations across the contiguous United States, which have a size of approximately 3° × 3°. For each subarray, we estimate slowness and backazimuth of the incoming wave, and use this information to calculate radial and transverse component beams from velocity seismograms that were bandpass-filtered retaining periods between 4 and 50 s. As suitable given the size of our subarrays, we use a curved wave front approach instead of the typical plane-wave approximation (Rost & Thomas 2009). To enhance slowness-backazimuth estimates, we measure how similar individual records are to the calculated beam, a quantity known as the *F*-statistic (Selby 2008; Frost *et al.* 2013). The maximum amplitude of the *F*-trace is used to infer the best-fitting slowness and backazimuth values. To be able to fairly compare waveforms and amplitudes between different components, we then calculate the linearly stacked beam using these slowness and backazimuth values for the unfiltered data.

We measure PcS beam splitting using SplitRacer, analogously to how we use it for PS and SKS splitting. We first apply a bandpass filter to our beamformed data, retaining periods between 4 and 25 s (Fig. 10d). This approach leads to robust splitting intensity measurements for most of the subarrays; however, we cannot obtain any well-constrained (ϕ, δt) measurements because splitting is generally weak, below the detection level for the transverse energy minimization method at these periods. However, the beamformed waveforms show clear PcS signals and relatively low noise levels. We therefore next measure splitting at frequencies that are higher than usual for shear-wave splitting measurements, retaining periods between 1-10 s (Fig. 10e). While the splitting intensity results are very similar to those obtained with the 4-25 s bandpass-filter, we successfully measure robust (ϕ, δt) splitting parameters for nine subarrays. The inclusion of higher frequency energy helps to resolve (ϕ, δt) because the time delay is larger compared to the dominant period of the signal. The measured (ϕ, δt) splitting parameters we obtain with this approach are similar to previously published ∗KS splitting measurements compiled in the IRIS shear-wave splitting database (IRIS DMC 2012).

Given this successful example, we suggest that PcS beam splitting measurements can be used in the future to fill in gaps in backazimuthal coverage that often exist for ∗KS measurements. PcS is useful because it is recorded at shorter distances than ∗KS (up to ∼63°) and therefore can largely increase the number of usable seismic events. A region for which PcS beam splitting measurements might be particularly helpful to improve backazimuthal coverage is Japan, which also has a densely spaced seismic stations suitable for beamforming, and which suffers from poor backazimuthal coverage for SK(K)S (Long & van der Hilst 2005). Further, we suggest that splitting measurements from beamformed data can generally be made at higher frequencies, which can increase the number of robust (ϕ, δt) measurements in cases of weak splitting, as shown in our example (Fig. 10e). The use of phases such as PcS that are recorded at a shorter distance than ∗KS also potentially has the effect that less high frequency energy is lost through attenuation along the ray path.

6 DISCUSSION

The results we obtained in our wavefield differencing approach show which parts of the seismic wavefield are sensitive to mantle seismic anisotropy. However, even if effects of mantle heterogeneity can be distinguished from seismic anisotropy, which is true for many cases (Fig. 8; e.g. Silver & Chan 1991; Long & Silver ; Nowacki *et al.* 2010; Romanowicz & Wenk 2017) but not all (e.g. Komatitsch *et al.* 2010; Borgeaud *et al.* 2016; Parisi *et al.* 2018; Wolf & Long 2024), it is not always straightforward to determine where along the ray path seismic anisotropy is located. For example, as demonstrated in Section 3, *S*-wave splitting can be strongly influenced by upper mantle anisotropy. This is why *S* is often used to characterize anisotropy near the earthquake source (e.g. Russo & Silver 1994; Foley & Long 2011; Walpole *et al.* 2017; Eakin *et al.* 2018). However, since there are limits to how reliable explicit corrections for receiver side anisotropy are Wolf *et al.* (2022b), the source-side *S*-wave splitting technique should be applied with caution.

While *S* is relatively simple because it samples the upper mantle only twice (once on the downgoing leg near the source and once on the upgoing leg near the receiver), other phases can be more complicated. For example, the SS phase potentially samples upper mantle anisotropy four times: at the source side, twice close to the reflection point, and beneath the receiver. This renders the phase practically unusable for inferring the precise geometry of upper mantle anisotropy in any particular location, although this has been tried (e.g. Wolfe & Silver 1998). Theoretically, upper mantle anisotropy should be known along three of the four legs of the ray path through the upper mantle to infer seismic anisotropy for the unknown leg, which is unrealistic for almost all possible source–receiver configurations. Alternatively, the sampled reflection point anisotropy could be assumed to be the same along the up- and downgoing leg for SS. Even if this assumption was justified, it would likely be practically impossible to reliably infer the anisotropy, at least using explicit ray-theory based corrections (Wolf *et al.* 2022b). This issue is applicable to any seismic phase that may be strongly influenced by mantle anisotropy and samples anisotropy in many separate locations. Therefore, while the splitting of phases such as SS, SSS, etc. may provide a general indication of the presence of seismic anisotropy along the ray path through analysis of their particle motions, they are not well suited to studying the precise geometry of anisotropy in any given region.

To infer lowermost mantle seismic anisotropy, we usually face a similar challenge. All phases that potentially sample lowermost mantle anisotropy also potentially sample seismic anisotropy in the upper mantle, which has to somehow be accounted for in studies of deep mantle anisotropy. Many of the phases that we have shown to be strongly influenced by lowermost mantle anisotropy (Section 3) are already commonly used to diagnose it. For example, SKS-SKKS differential splitting studies are common (e.g. Niu & Perez 2004; Reiss *et al.* 2019), *S* and ScS are often analyzed together to infer lowermost mantle anisotropy (Wookey *et al.* 2005; Nowacki *et al.* 2010; Wolf *et al.* 2019) and S_{diff} waves are also commonly used to infer lowermost mantle anisotropy (e.g. Vinnik *et al.* ; Cottaar & Romanowicz 2013; Wolf *et al.* 2023b). Our results do not clearly point to unusual phases that can be used to infer lowermost mantle anisotropy in future studies. While ScSScS unsurprisingly is strongly influenced by deep mantle anisotropy, it suffers from the same technical limitations as phases such as SS, SSS, etc., as discussed previously. Fig. 5 shows that beyond around 120°, PS starts to be influenced by lowermost mantle anisotropy. However, it is unclear how this could be exploited in practice. In theory, a PS-PScS differential splitting technique could be applied in an analogous manner to S-ScS differential splitting. However, a complication is that PS and PScS do not generally have the same reflection point at the surface. Therefore, splitting close to the reflection point would be hard to characterize for PScS, making it impossible to distinguish it from a lowermost mantle contribution.

7 FUTURE DIRECTIONS

Our wavefield differencing results point towards new strategies to measure and characterize seismic anisotropy using shear-wave splitting observations, two of which we demonstrated as proof-of-concept examples. In order to identify the region of the mantle from which a splitting signal originates, the wave should (ideally) not sample seismic anisotropy in multiple different locations along the ray path. Additionally, to enable splitting analysis the initial polarization of the wave should be known. These two conditions are satisfied for the two novel splitting strategies we explore here: PS-SKS differential splitting and PcS beam splitting. SKS, PS and PcS all involve initially SV-polarized *S* waves due to the *P*-SV conversion either at the CMB or at the surface.

PcS phases do not usually have high amplitudes (Liu & Grand 2018), which is why it is helpful to use these waves in a beamforming framework. We suggest that it is often more helpful to measure splitting for seismic phases with lower amplitudes, for which it is straightforward to understand where along the ray path mantle anisotropy is sampled, than seismic phases that may be strongly influenced by mantle anisotropy, but in a complicated manner (for example, SS). Such low amplitude seismic phases can be enhanced using array techniques, making use of the fact that the splitting parameters measured from beams or stacks approximately agree with the average splitting parameters of the single-station seismograms contributing to them (Wolf *et al.* 2023a). Such an approach has been applied to S3KS previously (Wolf *et al.* 2023a) and to relatively high-frequency PcS in this work. Based on these findings, we suggest to apply beamforming routinely in studies that measure shear-wave splitting. For example, Fig. 5 shows that there are minor arc seismic phases affected by lowermost mantle anisotropy. Such phases, like minor arc SKKS or S3KS, can be used for measurements of mantle anisotropy more commonly than they currently are. Similarly, the measurement of differential PPS-SKS or PPS-SKKS

splitting is conceivable, by enhancing signals via beamforming if necessary. Such new splitting strategies involving minor arc phases and unusual source–receiver configurations will be helpful to infer upper mantle anisotropy in locations that suffer from poor coverage, as well as to study lowermost mantle anisotropy, which is often only detectable for specific ray path configurations.

8 CONCLUSION

In this work, we have applied a wavefield differencing approach to analyze the differences between wavefield for isotropic and anisotropic models, incorporating seismic anisotropy at different mantle depths. These wavefield differencing results demonstrate which seismic phases are most strongly influenced by mantle anisotropy. We show that some seismic phases are more suitable than others to infer splitting, even if they are influenced by mantle anisotropy to a similar degree. In particular, we suggest that the PS-SKS differential splitting technique can be commonly used to infer upper mantle seismic anisotropy beneath ocean basins, based on a proof-of-concept example using a station in Canada and earthquakes in the western Pacific. Additionally, seismic phases that are not usually used for splitting measurements because of their low amplitudes should be more routinely analyzed in areas of dense seismic array deployments using a beamforming approach. As a proof-of-concept example, we calculate high-frequency PcS beam splitting for one seismic event for stations across the United States. The wavefield differencing results presented here may inform the design of future studies of mantle anisotropy using body waves.

ACKNOWLEDGMENTS

This work was funded by Yale University and by the U.S. National Science Foundation via grant EAR-2026917 to MDL and grant EAR-2027181 to DAF. We thank the Yale Center for Research Computing for providing the necessary research computing infrastructure for this study. The Generic Mapping Tools (Wessel & Smith 1998) and ObsPy (Beyreuther *et al.* 2010) were used in this research. We thank editor Ana Ferreira and two anonymous reviewers for constructive comments that helped us to improve the paper. We are grateful for discussions with Regina Maass.

SUPPORTING INFORMATION

Supplementary data are available at *GJI* online.

suppl_data

Please note: Oxford University Press is not responsible for the content or functionality of any supporting materials supplied by the authors. Any queries (other than missing material) should be directed to the corresponding author for the paper.

DATA AVAILABILITY

The synthetic seismograms for this study were computed using AxiSEM3D (Leng *et al.* 2016, 2019), which is publicly available at https://github.com/AxiSEMunity (Fernando *et al.* 2024).

The stations across the United States used for beamforming of PcS have the following network codes: AR, AZ (UC San Diego 1982), BK (Northern California Earthquake Data Center 2014), CC (Cascades Volcano Observatory/USGS 2001), CI (California Institute of Technology and United States Geological Survey Pasadena 1926), CN (Natural Resources Canada (NRCAN Canada) 1975), CU (Albuquerque Seismological Laboratory (ASL)/USGS 2006), EP, GS (Albuquerque Seismological Laboratory (ASL)/USGS 1980), HW, II (Scripps Institution of Oceanography 1986), IM, IU (Albuquerque Seismological Laboratory/USGS 2014), IW (Albuquerque Seismological Laboratory (ASL)/USGS 2003), LB, LD (Lamont Doherty Earth Observatory (LDEO), Columbia University 1970), NE (Albuquerque Seismological Laboratory (ASL)/USGS 1994), NM, PE (Penn State University 2004), SC, TA (IRIS Transportable Array 2003), UO (University of Oregon 1990), US (Albuquerque Seismological Laboratory (ASL)/USGS 1990), UW (University of Washington 1963), XO (Gary Pavlis & Hersh Gilbert 2011), Y5, YX (Simon Klemperer & Kate Miller 2010) and Z9 (Fischer *et al.* 2010). The station used for the PS splitting measurements is INK (Natural Resources Canada (NRCAN Canada) 1975). All data are publicly available.

REFERENCES

Albuquerque Seismological Laboratory (ASL)/USGS, 1980. US Geological Survey Net-works [Data set]. https://doi.org/10.7914/SN/GS

Albuquerque Seismological Laboratory (ASL)/USGS, 1990. United States National Seismic Network [Data set]. https://doi.org/10.7914/SN/US

Albuquerque Seismological Laboratory (ASL)/USGS, 1994. New England Seismic Network [Data set].https://doi.org/10.7914/SN/NE

Albuquerque Seismological Laboratory (ASL)/USGS, 2003. Intermountain West SeismicNetwork [Data set]. https://doi.org/10.7914/SN/IW

Albuquerque Seismological Laboratory (ASL)/USGS, 2006. Caribbean Network [Data set]. https://doi.org/10.7914/SN/CU

Albuquerque Seismological Laboratory/USGS, 2014. Global Seismograph Network (GSN- IRIS/USGS) [Data set]. https://doi.org/10.7914/SN/IU

Asplet, J., Wookey, J. & Kendall, M., 2020. A potential post-perovskite province in D″ beneath the Eastern Pacific: evidence from new analysis of discrepant SKS–SKKS shear-wave splitting, *Geophys. J. Int.,* **221,** 2075–2090.

Becker, T. W., 2020. Seismic anisotropy, in *Encyclopedia of Solid Earth Geophysics,* pp. 1–11, Springer.

Becker, T.W. & Lebedev, S., 2021. *Dynamics of the Upper Mantle in Light of Seismic Anisotropy,* Chap. 10, pp. 257–282, American Geophysical Union. doi: 10.1002/9781119528609.ch10.

Beyreuther, M., Barsch, R., Krischer, L., Megies, T., Behr, Y. & Wassermann, J., 2010. Obspy: a python toolbox for seismology, *Seismol. Res. Lett.,* **81,** 530–533.

Borgeaud, A.F., Konishi, K., Kawai, K. & Geller, R.J., 2016. Finite frequency effects on apparent S-wave splitting in the D″ layer: comparison between ray theory and full-wave synthetics, *Geophys. J. Int.,* **207,** 12–28.

California Institute of Technology and United States Geological Survey Pasadena, 1926. Southern California Seismic Network [Data set]. https://doi.org/10.7914/SN/CI.

Cascades Volcano Observatory/USGS, 2001. Cascade Chain Volcano Monitoring [Data set]. https://doi.org/10.7914/SN/CC.

Chang, S.-J. & Ferreira, A. M.G., 2019. Inference on water content in the mantle transition zone near subducted slabs from anisotropy tomography, *Geochem. Geophys. Geosyst.,* **20,** 1189–1201.

Chevrot, S., 2000. Multichannel analysis of shear wave splitting, *J. geophys. Res.,* **105,** 21579–21590.

Cottaar, S. & Romanowicz, B., 2013. Observations of changing anisotropy across the southern margin of the African LLSVP, *Geophys. J. Int.,* **195,** 1184–1195.

Creasy, N., Long, M.D. & Ford, H.A., 2017. Deformation in the lowermost mantle beneath Australia from observations and models of seismic anisotropy, *J. geophys. Res.,* **122,** 5243–5267.

Deng, J., Long, M.D., Creasy, N., Wagner, L., Beck, S., Zandt, G., Tavera, H. & Minaya, E., 2017. Lowermost mantle anisotropy near the eastern edge of the Pacific LLSVP: constraints from SKS-SKKS splitting intensity measurements, *Geophys. J. Int.,* **210,** 774–786.

Dziewonski, A.M. & Anderson, D.L., 1981. Preliminary reference Earth model, *Phys. Earth planet. Inter.,* **25,** 297–356.

Eakin, C., Rychert, C. & Harmon, N., 2018. The role of oceanic transform faults in seafloor spreading: a global perspective from seismic anisotropy, *J. geophys. Res.,* **123,** 1736–1751.

Favier, N., Chevrot, S. & Komatitsch, D., 2004. Near-field influence on shear wave splitting and traveltime sensitivity kernels, *Geophys. J. Int.,* **156**(3), 467–482.

Fernando, B., Wolf, J., Nissen-Meyer, T., Eaton, W., Styczinski, M., Walker, A., Craig, T., Muir, J., Nunn, C. & Long, M.D. 2024. *AxiSEM3D - An Introduction to Using the Code and its Applications,* doi: 10.31223/X5TH7P.

Ferreira, A. M.G., Woodhouse, J.H., Visser, K. & Trampert, J., 2010. On the robustness of global radially anisotropic surface wave tomography, *J. geophys. Res.,* **115**(B4), B04313.

Fischer, K.M., Hawman, R.B. & Wagner, L.S., 2010. Southeastern Suture of the Appalachian Margin Experiment [Data set]. International Federation of Digital Seismograph Networks. https://doi.org/10.7914/SN/Z9_2010.

Foley, B.J. & Long, M.D., 2011. Upper and mid–mantle anisotropy beneath the Tonga slab, *Geophys. Res. Lett.,* **38**(2), doi: 10.1029/2010GL046021.

Fontaine, F.R., Barruol, G., Tommasi, A. & Bokelmann, G. H.R., 2007. Upper-mantle flow beneath French Polynesia from shear wave splitting, *Geophys. J. Int.,* **170,** 1262–1288.

French, S.W. & Romanowicz, B.A., 2014. Whole-mantle radially anisotropic shear velocity structure from spectral-element waveform tomography, *Geophys. J. Int.,* **199**(3), 1303–1327.

Frost, D.A., Rost, S., Selby, N. & Stuart, G., 2013. Detection of a tall ridge at the core-mantle boundary from scattered PKP energy, *Geophys. J. Int.,* **195**(1), 558–574.

Frost, D.A., Garnero, E., Creasy, N., Wolf, J., Bozdag, E., Long, M., Aderoju, A. & Vite, R., 2024. Heterogeneous mantle effects on the behavior of SmKS waves and outermost core imaging, *Geophys. J. Int.*.**237**(3), 1655–1673.

Pavlis, G. & Gilbert, H., 2011. Ozark Illinois Indiana Kentucky (OIINK) Flexible Array Experiment [Data set]. International Federation of Digital Seismograph Networks. https://doi.org/10.7914/SN/XO_2011.

Graw, J.H. & Hansen, S.E., 2017. Upper mantle seismic anisotropy beneath the Northern Transantarctic Mountains, Antarctica from PKS, SKS, and SKKS splitting analysis, *Geochem. Geophys. Geosyst.,* **18,** 544–557.

Grund, M. & Ritter, J.R., 2018. Widespread seismic anisotropy in Earth's lowermost mantle beneath the Atlantic and Siberia, *Geology,* **47,** 123–126.

Haws, A.A., Long, M.D. & Luo, Y., 2023. Anisotropic structure of the normally-dipping and flat slab segments of the Alaska subduction zone: insights from receiver function analysis, *Tectonophysics,* **868,** 230112. doi: 10.1016/j.tecto.2023.230112.

He, X. & Long, M.D., 2011. Lowermost mantle anisotropy beneath the northwestern Pacific: evidence from PcS, ScS, SKS, and SKKS phases, *Geochem. Geophys. Geosyst.,* **12**(12),Q12012. doi: 10.1029/2011GC003779.

IRIS DMC, 2012. Data Services Products: SWS-DBs Shear-wave splitting databases, https://doi.org/10.17611/DP/SWS.1.

IRIS Transportable Array, 2003. USArray Transportable Array [Data set]. International Federation of Digital Seismograph Networks. https://doi.org/10.7914/SN/TA.

Kawai, K. & Geller, R.J., 2010. Waveform inversion for localized seismic structure and an application to D" structure beneath the Pacific, *J. geophys. Res.,* **115**(B1), B01305. doi: 10.1029/2009JB006503.

Komatitsch, D., Vinnik, L.P. & Chevrot, S., 2010. SHdiff-SVdiff splitting in an isotropic Earth, *J. geophys. Res.,* **115**(B7), doi: 10.1029/2009JB006795.

Lamont-Doherty Earth Observatory (LDEO), 1970. Lamont-Doherty Cooperative Seismographic Network, Columbia University, https://doi.org/10.7914/SN/LD.

Leng, K., Nissen-Meyer, T. & van Driel, M., 2016. Efficient global wave propagation adapted to 3-D structural complexity: a pseudospectral/spectral-element approach, *Geophys. J. Int.,* **207**(3), 1700–1721.

Leng, K., Nissen-Meyer, T., van Driel, M., Hosseini, K. & Al-Attar, D., 2019. AxiSEM3D: broad-band seismic wavefields in 3-D global earth models with undulating discontinuities, *Geophys. J. Int.,* **217**(3), 2125–2146.

Levin, V. & Park, J., 1997. P-SH conversions in a flat-layered medium with anisotropy of arbitrary orientation, *Geophys. J. Int.,* **131**(2), 253–266.

Liu, C. & Grand, S.P., 2018. Seismic attenuation in the African LLSVP estimated from PcS phases, *Earth planet. Sci. Lett.,* **489,** 8–16.

Liu, K. *et al.*, 2014. A uniform database of teleseismic shear wave splitting measurements for the western and central United States, *Geochem. Geophys. Geosyst.,* **15,** 2075–2085.

Long, M.D. & Becker, T., 2010. Mantle dynamics and seismic anisotropy, *Earth planet. Sci. Lett.,* **297,** 341–354.

Long, M.D. & Silver, P.G., 2009. Shear wave splitting and mantle anisotropy: measurements, interpretations, and new directions, *Surv. Geophys.,* **30,** 407–461.

Long, M.D. & van der Hilst, R.D., 2005. Upper mantle anisotropy beneath Japan from shear wave splitting, *Phys. Earth planet. Inter.,* **151**(3), 206–222.

Lopes, E., Long, M.D., Karabinos, P. & Aragon, J.C., 2020. SKS splitting and upper mantle anisotropy beneath the Southern New England Appalachians: constraints from the dense SEISConn array, *Geochem. Geophys. Geosyst.,* **21,** e2020GC009401. doi: 10.1029/2020GC009401.

Lynner, C., 2021. Anisotropy-revealed change in hydration along the Alaska subduction zone, *Geology,* **49**(9), 1122–1125.

Lynner, C. & Long, M.D., 2013. Sub-slab seismic anisotropy and mantle flow beneath the Caribbean and Scotia subduction zones: effects of slab morphology and kinematics, *Earth planet. Sci. Lett.,* **361,** 367–378.

Lynner, C. & Long, M.D., 2015. Heterogeneous seismic anisotropy in the transition zone and uppermost lower mantle: evidence from South America, Izu-Bonin and Japan, *Geophys. J. Int.,* **201,** 1545–1552.

Meade, C., Silver, P.G. & Kaneshima, S., 1995. Laboratory and seismological observations of lower mantle isotropy, *Geophys. Res. Lett.,* **22,** 1293–1296.

Mohiuddin, A., Long, M.D. & Lynner, C., 2015. Mid-mantle seismic anisotropy beneath Southwestern Pacific subduction systems and implications for mid-mantle deformation, *Phys. Earth planet. Inter.,* **245,** 1–14.

Mondal, P. & Long, M.D., 2020. Strong seismic anisotropy in the deep upper mantle beneath the Cascadia backarc: constraints from probabilistic finite-frequency SKS splitting intensity tomography, *Earth planet. Sci. Lett.,* **539,** 116172. doi: 10.1016/j.epsl.2020.116172.

Murdie, R.E. & Russo, R.M., 1999. Seismic anisotropy in the region of the Chile margin triple junction, *J. South Am. Earth Sci.,* **12,** 261–270.

Natural Resources Canada (NRCAN Canada), 1975. Canadian National Seismograph Network [Data set]. International Federation of Digital Seismograph Networks. https://doi.org/10.7914/SN/CN.

Nikulin, A., Levin, V. & Park, J., 2009. Receiver function study of the Cascadia megathrust: evidence for localized serpentinization, *Geochem. Geophys. Geosyst.,* **10**(7), Q07004. doi: 10.1029/2009GC002376.

Nissen-Meyer, T., van Driel, M., Stähler, S.C., Hosseini, K., Hempel, S., Auer, L., Colombi, A. & Fournier, A., 2014. AxiSEM: broadband 3-D seismic wavefields in axisymmetric media, *Solid Earth,* **5,** 425–445.

Niu, F. & Perez, A.M., 2004. Seismic anisotropy in the lower mantle: a comparison of waveform splitting of SKS and SKKS, *Geophys. Res. Lett.,* **31**(24), L24612. doi: 10.1029/2004GL021196.

Northern California Earthquake Data Center, 2014. Berkeley Digital Seismic Network (BDSN) [Data set]. Northern California Earthquake Data Center. https://doi.org/10.7932/BDSN.

Nowacki, A. & Wookey, J., 2016. The limits of ray theory when measuring shear wave splitting in the lowermost mantle with ScS waves, *Geophys. J. Int.,* **207,** 1573–1583.
Nowacki, A., Wookey, J. & Kendall, J.-M., 2010. Deformation of the lowermost mantle from seismic anisotropy., *Nature,* **467,** 1091–1094.
Panning, M.P. & Nolet, G., 2008. Surface wave tomography for azimuthal anisotropy in a strongly reduced parameter space, *Geophys. J. Int.,* **174**(2), 629–648.
Parisi, L., Ferreira, A. M.G. & Ritsema, J., 2018. Apparent splitting of S waves propagating through an isotropic lowermost mantle, *J. geophys. Res.,* **123,** 3909–3922.
Penn State University, 2004. Pennsylvania State Seismic Network [Data set]. International Federation of Digital Seismograph Networks. https://doi.org/10.7914/SN/PE.
Reiss, M. & Rümpker, G., 2017. SplitRacer: MATLAB code and GUI for semiautomated analysis and interpretation of teleseismic shear-wave splitting, *Seismol. Res. Lett.,* **88,** 392–409.
Reiss, M.C., Long, M.D. & Creasy, N., 2019. Lowermost mantle anisotropy beneath Africa from differential SKS-SKKS shear-wave splitting, *J. geophys. Res.,* **124**(8), 8540–8564.
Ritsema, J., Deuss, A., van Heijst, H.J. & Woodhouse, J.H., 2011. S40RTS: a degree-40 shear-velocity model for the mantle from new Rayleigh wave dispersion, teleseismic traveltime and normal-mode splitting function measurements, *Geophys. J. Int.,* **184**(3), 1223–1236.
Romanowicz, B. & Wenk, H.-R., 2017. Anisotropy in the deep Earth, *Phys. Earth planet. Inter.,* **269,** 58–90.
Rost, S. & Thomas, C., 2009. Improving seismic resolution through array processing techniques, *Surv. Geophys.,* **30,** 271–299.
Russo, R.M. & Silver, P.G., 1994. Trench-parallel flow beneath the Nazca plate from seismic anisotropy, *Science,* **263**(5150), 1105–1111.
Savage, M.K., 1999. Seismic anisotropy and mantle deformation: what have we learned from shear wave splitting?, *Rev. Geophys.,* **37,** 65–106.
Schulte-Pelkum, V., Monsalve, G., Sheehan, A., Pandey, M., Sapkota, S., Bilham, R. & Wu, F., 2005. Imaging the Indian Subcontinent beneath the Himalaya, *Nature,* **435,** 1222–1225.
Scripps Institution of Oceanography, 1986. Global Seismograph Network - IRIS/IDA [Data set]. International Federation of Digital Seismograph Networks. https://doi.org/10.7914/SN/II.
Selby, N.D., 2008. Application of a generalized F detector at a seismometer array, *Bull. seism. Soc. Am.,* **98**(5), 2469–2481.
Sieminski, A., Liu, Q., Trampert, J. & Tromp, J., 2007. Finite–frequency sensitivity of surface waves to anisotropy based upon adjoint methods, *Geophys. J. Int.,* **168,** 1153–1174.
Sieminski, A., Paulssen, H., Trampert, J. & Tromp, J., 2008. Finite-frequency SKS splitting: measurement and sensitivity kernels, *Bull. seism. Soc. Am.,* **98,** 1797–1810.
Silver, P.G., 1996. Seismic anisotropy beneath the continents: probing the depths of geology, *Ann. Rev. Earth planet. Sci.,* **24**(1), 385–432.
Silver, P.G. & Chan, W.W., 1991. Shear wave splitting and subcontinental mantle deformation, *J. geophys. Res.,* **96,** 429–454.
Klemperer, S. & Miller, K., 2010. Flexarray 3D Passive Seismic Imaging of Core-Complex Extension in the Ruby Range Nevada [Data set]. International Federation of Digital Seismograph Networks. https://doi.org/10.7914/SN/YX_2010.
Su, L. & Park, J., 1994. Anisotropy and the splitting of PS waves, *Phys. Earth planet. Inter.,* **86,** 263–276.
Suzuki, Y., Kawai, K. & Geller, R.J., 2021. Imaging paleoslabs and inferring the Clapeyron slope in D" beneath the northern Pacific based on high-resolution inversion of seismic waveforms for 3-D transversely isotropic structure, *Phys. Earth planet. Inter.,* **321,** doi: 10.1016/j.pepi.2021.106751.
Tesoniero, A., Leng, K., M., D.Long & Nissen-Meyer, T., 2020. Full wave sensitivity of SK(K)S phases to arbitrary anisotropy in the upper and lower mantle, *Geophys. J. Int.,* **222**(1), 412–435.
UC San Diego, 1982. ANZA Regional Network [Data set]. International Federation of Digital Seismograph Networks. https://doi.org/10.7914/SN/AZ.
University of Oregon, 1990. Pacific Northwest Seismic Network - University of Oregon [Data set]. International Federation of Digital Seismograph Networks. https://doi.org/10.7914/SN/UO.
University of Washington, 1963. Pacific Northwest Seismic Network - University of Washington [Data set]. International Federation of Digital Seismograph Networks. https://doi.org/10.7914/SN/UW.
Vinnik, L., Farra, V. & Romanowicz, B., 1989a. Azimuthal anisotropy in the earth from observations of SKS at GEOSCOPE and NARS broadband stations, *Bull. seism. Soc. Am.,* **79,** 1542–1558.
Vinnik, L., Romanowicz, B., Le Stunff, Y. & Makeyeva, L., 1995. Seismic anisotropy in the D″ layer, *Geophys. Res. Lett.,* **22**(13), 1657–1660.
Vinnik, L., Farra, V. & Romanowicz, B., 1989. Observational evidence for diffracted SV in the shadow of the Earth's core, *Geophys. Res. Lett.,* **16**(6), 519–522.
Walker, A. & Wookey, J., 2012. MSAT - a new toolkit for the analysis of elastic and seismic anisotropy, *Comput. Geosci.,* **49,** 81–90.
Walpole, J., Wookey, J., Masters, G. & Kendall, J.M., 2014. A uniformly processed data set of SKS shear wave splitting measurements: a global investigation of upper mantle anisotropy beneath seismic stations, *Geochem. Geophys. Geosyst.,* **15,** 1991–2010.
Walpole, J., Wookey, J., Kendall, J.-M. & Masters, T.-G., 2017. Seismic anisotropy and mantle flow below subducting slabs, *Earth planet. Sci. Lett.,* **465,** 155–167.
Walsh, E., Arnold, R. & Savage, M.K., 2013. Silver and Chan revisited, *J. geophys. Res.,* **118,** 5500–5515.
Wessel, P. & Smith, W. H.F., 1998. New, improved version of generic mapping tools released, *EOS, Trans. Am. geophys. Un.,* **79,** 579–579.
Wolf, J. & Long, M., 2024. Splitting of ScS waves due to lowermost mantle anisotropy: practical challenges and new global measurements, *Seismica,* **3**(1), doi: 10.26443/seismica.v3i1.1128.
Wolf, J. & Long, M.D., 2023a. Upper mantle anisotropy and flow beneath the Pacific Ocean revealed by differential PS-SKS splitting, *Geophys. Res. Lett.,* **50**(16), e2023GL104402. doi: 10.1029/2023GL104402
Wolf, J. & Long, M.D., 2023b. Lowermost mantle structure beneath the central Pacific Ocean: ultralow velocity zones and seismic anisotropy, *Geochem. Geophys. Geosyst.,* **24,** e2022GC010853. doi: 10.1029/2022GC010853
Wolf, J., Creasy, N., Pisconti, A., Long, M.D. & Thomas, C., 2019. An investigation of seismic anisotropy in the lowermost mantle beneath Iceland, *Geophys. J. Int.,* **219**(Suppl 1), S152–S166.
Wolf, J., Long, M.D., Leng, K. & Nissen-Meyer, T., 2022a. Sensitivity of SK(K)S and ScS phases to heterogeneous anisotropy in the lowermost mantle from global wavefield simulations, *Geophys. J. Int.,* **228,** 366–386.
Wolf, J., Long, M.D., Leng, K. & Nissen-Meyer, T., 2022b. Constraining deep mantle anisotropy with shear wave splitting measurements: challenges and new measurement strategies, *Geophys. J. Int.,* **230,** 507–527.
Wolf, J., Frost, D.A., Long, M.D., Garnero, E., Aderoju, A.O., Creasy, N. & Bozdağ, E., 2023a. Observations of mantle seismic anisotropy using array techniques: shear-wave splitting of beamformed SmKS phases, *J. geophys. Res.,* **128**(1), e2022JB025556. doi: 10.1029/2022JB025556
Wolf, J., Long, M.D., Creasy, N. & Garnero, E., 2023b. On the measurement of Sdiff splitting caused by lowermost mantle anisotropy, *Geophys. J. Int.,* **233**(2), 900–921.
Wolf, J., Long, M.D., Li, M. & Garnero, E., 2023c. Global compilation of deep mantle anisotropy observations and possible correlation with low velocity provinces, *Geochem. Geophys. Geosyst.,* **24**(10), e2023GC011070. doi: 10.1029/2023GC011070
Wolf, J., Li, M., Long, M. & Garnero, E., 2024a. Advances in mapping lowermost mantle convective flow with seismic anisotropy observations, *Rev. Geophys*. doi: 10.1029/2023RG000833
Wolf, J., Long, M.D. & Frost, D.A., 2024b. Ultralow velocity zone and deep mantle flow beneath the Himalayas linked to subducted slab, *Nat. Geosci.,* **17,** 302–308.
Wolfe, C.J. & Silver, P.G., 1998. Seismic anisotropy of oceanic upper mantle: shear wave splitting methodologies and observations, *J. geophys. Res.,* **103**(B1), 749–771.

Wookey, J., Kendall, J.-M. & Rümpker, G., 2005. Lowermost mantle anisotropy beneath the north Pacific from differential S-ScS splitting, *Geophys. J. Int.,* **161,** 829–838.

Yuan, K. & Beghein, C., 2014. Three-dimensional variations in Love and Rayleigh wave azimuthal anisotropy for the upper 800km of the mantle, *J. geophys. Res.,* **119,** 3232–3255.

Zhu, H., Yang, J. & Li, X., 2020. Azimuthal anisotropy of the North American upper mantle based on full waveform inversion, *J. geophys. Res.,* **125**(2), e2019JB018432. doi: 10.1029/2019JB018432

Zietlow, D.W., Sheehan, A.F., Molnar, P.H., Savage, M.K., Hirth, G., Collins, J.A. & Hager, B.H., 2014. Upper mantle seismic anisotropy at a strike-slip boundary: South Island, New Zealand, *J. geophys. Res.,* **119,** 1020–1040.